Universidad de Valladolid

Escuela de Doctorado

Trabajo Fin de Máster

Máster en Física

Reactivity and oxidation of Fe_xNi_{13-x} nanoalloys

Autor: Guillermo Vinuesa Sanz

Tutor: Andrés Vega Hierro

Reactivity and oxidation of Fe_xNi_{13-x} nanoalloys

Author: G. Vinuesa-Sanz[1] and Advisor: A. Vega[1]

Departamento de Física Teórica, Atómica y Óptica, Universidad de Valladolid, E-47011 Valladolid, Spain.

(Dated: 24 June 2019)

Abstract

First-principles calculations were conducted for charged iron-nickel nanoalloys to study their structural and electronic properties. These can help in determining their reactivity and stability, to asses if they are good candidates as catalysts for some chemical reactions, and to determine optimal geometries and chemical compositions in this context. We calculated global reactivity indicators (such as electronegativity) that allow us to foresee the best chemical compositions for oxidation, and local reactivity indicators (Fukui functions) that predict which sites of the clusters are, on average, the most reactive ones. Oxygen absorption calculations for the most and least electronegative clusters have also been made to find out which sites are the optimal for oxygen molecules adsorption.

Se han realizado cálculos de primeros principios para estudiar la propiedades estructurales y electrónicas de las nanoaleaciones de hierro-níquel cargadas positiva y negativamente, $Fe_xNi^{\pm}_{13-x}$, para determinar su reactividad y estabilidad, y así evaluar si son buenas candidatas como catalizadores para ciertas reacciones químicas, identificando sus geometrías óptimas y composiciones químicas en este contexto. Se han calculado índices de reactividad global (como la electronegatividad) que nos permiten prever las mejores composiciones químicas para la oxidación, e índices de reactividad local (funciones de Fukui) que predicen que sitios de los clusters son mas reactivos en promedio. También se han llevado a cabo cálculos de absorción de oxígeno para los clusters mas y menos electronegativos, a fin de hallar las posiciones óptimas del cluster para la adsorción del oxígeno.

Keywords: Density functional theory, nanoalloys, nanoreactivity, electronic structure, catalyst

I. INTRODUCTION

The experimental and theoretical study of nanoparticles is of great relevance in Materials Science. Nanoparticle properties are strongly size-dependant and their geometry and electronic structure determine their reactivity, magnetic, thermal or optical properties. At the nano-scale, quantum effects due to quantum confinement arise, causing the nanoparticles to have different properties from those of their isolated atoms and bulk counterparts[1]. For example, the catalytic properties increase with the exposed surface of the material. Nanoparticles are interesting as catalysts for that very reason, their large surface/volume ratio simulates local atomic and chemical environments of extensive granular systems.

Among all nanoparticles, one of the most interesting are transition metals' nanoalloys. When we mix two or more metals at the macroscale, the result is an alloy, a material with improved physical and/or chemical properties, such as stainless steel (Fe - Cr). In nanoalloy clusters, physical and chemical properties depend greatly on the numbers of atoms of each atomic species and on the chemical ordering, not only on their size. These extra variables give nanoalloys a great variety of structural and electronic properties[1], which makes them an interesting and challenging case for study.

Some experimental data show that iron-nickel oxide, as well as big particles of Fe with certain amounts of Ni on their surface, have better performance than pure iron oxides for decomposition reactions of organic pollutants[2]. Park et al.[3] discovered that composition of the iron-nickel catalysts has an enormous effect on the decomposition reaction of the CO and H_2 mixture at 600°C. This goes to show that, as the fraction of nickel increases in an iron nickel catalyst, there is a 70% decrease in the CO conversion. Their next study[4] proved the same strong composition dependence of this catalyst for the decomposition reaction in Ethylene-Hydrogen mixtures, showing how a 5% nickel increase in a FeNi catalyst resulted in a great improvement in the conversion of ethylene from 13% to 52%.

A lot of recent studies have focused on the reactivity properties of iron-nickel sulfide nanosheets[5] and iron-nickel nitride nanosheets[6], nanoarrays[7] and nanostructures[8], showing their efficiency as catalysts in oxygen and hydrogen evolution reactions, also known

as OER and HER. Because of this, FeNi-N and FeNi-S nanostructures are good candidates as bifunctional electrocatalysts for overall water splitting, which is a promising form of clean and efficient energy production. In the same context, Hu et al[9] showed that several compositions of Fe-Ni deposits exhibit good activities as catalysts of OER and HER, when employed as electrode materials for water electrolysis at high current densities. This means that they could be used as electrocatalyst materials for bipolar water electrolysers. More recently, iron nickel oxides have also proven to be more efficient electrocatalysts than pure nickel oxides for solar[10] and alkaline[11] water splitting.

Despite all the research focused on the applications of iron-nickel systems and nanostructures as catalysts, their reactivity properties have not been studied in detail with a quantum mechanics approach, so as to get insight on the fundamental aspects that explain their behaviour. That is the main goal of this work, to determine the foremost reactivity indicators (both global and local) of FeNi alloy nanoparticles, and the most fundamental aspects of the first stage of their oxidation.

As a first step in the understanding of the reactivity of Fe-Ni nanoalloys, this study focus on the 13 atoms nanoalloy across all the concentration range, whose ground state structural properties in the non-charged state were studied in our previous work[12]. Electronic and magnetic properties were studied and, as a first approach to the reactivity, the density of states (both total and projected) was studied determining its HOMO and LUMO states. Furthermore, global and local reactivity indicators are calculated and analysed.

Prior to explicitly determining any global or local reactivity index, we examine the structural and electronic properties of the charged nanoalloys (both positive and negative states), paying particular attention to their magnetic moment and charge transfer properties, making a comparison with the neutral states. Then, both global and local reactivity indicators are studied in order to asses the reactivity of the nanoalloys. Finally, an study of O_2 adsorption on the most and less electronegative nanoalloys is carried out.

This paper is structured as follows. In Section II, we briefly describe the theoretical approach. Then, in Section III, we present the results. Section III.A reports the structures of the putative global minima as well as their energetic stability. In Section III.B we discuss the magnetic properties and charge transfer effects. Section III.C provides a discussion on the expected reactivity of selected nanoalloys based on global and local conceptual density functional theory indicators, such as electronegativity (global) and the Fukui function (local). In section III.D we discuss the results of oxygen adsorption. Finally, the main results are summarized in the concluding section IV.

We provide supplementary information (SI) in Section VI about low energy structural isomers for the different nanoalloys and states of charge.

II. THEORETICAL MODEL

We performed the calculations with the Density Functional Theory (DFT[13]) framework as implemented in the VASP (Vienna Ab Initio Simulation package)[14,15,16,17] code, using the generalized gradient approximation (GGA) of Perdew, Burke and Ernzerhof (PBE)[18] to treat the exchange-correlation effects. VASP is a plane-wave code that solves the spin-polarized Kohn–Sham equations[19] within the projector-augmented wave (PAW) approach[20,21,22]. The PAW method allows for a considerable reduction of the number of plane-waves per atom for transition metals and first row elements, and provides a more accurate representation of the effects of core electrons as compared to pseudopotentials.

The technical settings in the calculations were as follows. The clusters were placed in a cubic cell of $25 \times 25 \times 25$ Å^3, large enough to make the interaction between the cluster and its replicas in neighboring cells negligible. Thus, only the gamma (Γ) point (k=0) was considered when integrating over the Brillouin zone, as it is usual for finite systems. The structures were relaxed until the force on each atom was smaller than 0.005 eV/Å, and the plane wave cutoff was 350 eV. In every calculation, an energy convergence criterion of 10^{-6} for the electronic density was used.

To calculate geometries of the ground state, and first low-energy isomers for each concentration in the charged 13 atoms Fe-Ni nanoparticles, we follow a similar computational strategy to the already seen in our previous work[12], about the 13 atom neutral Fe-Ni nanoalloys. We select as trial structures the four more stable ones that were determined in our previous work for the neutral nanoalloys. As a first step, we re-optimize them at the Density Functional Theory (DFT) level. After this structural relaxation we can compare the resulting geometries and their stabilities with the neutral ones, and see if the ground state geometry of a particular composition has changed with the addition or removal of one electron. Calculations of the vertical (only electronic relaxation) and adiabatic (electronic and ionic relaxation) ionization potential and electron affinities were performed.

To determine local electronic charges and magnetic moments, we made use of the Bader[23] method, which is based on the division of the cluster in several atomic volumes. This is accomplished by locating the zero-flux sur-

faces of the electron density field. We used this method as implemented in an efficient open source code thanks to the group of Henkelman[24]. Using this method we ensure that the sum of the electronic charges at each atom of the cluster recover the total electronic charge, which is not the case when projecting plane waves onto spherical volumes. To properly identify the electron density maxima at the nuclear sites, the Bader analysis is performed on the total electron density, extracting the core charge from the PAW calculations, and adding it to the valence charge.

A. Energetic stability indicators

As a measure of the nanoalloy stability of each cluster, we evaluated the excess energy, defined as:

$$E_{exc}(Fe_xNi^{\pm}_{13-x}) = E(Fe_xNi^{\pm}_{13-x}) - x\frac{E(Fe^{\pm}_{13})}{13} - (13-x)\frac{E(Ni^{\pm}_{13})}{13} \quad (1)$$

where $E(Fe^{\pm}_{13})$ and $E(Ni^{\pm}_{13})$ are the energies of the pure clusters in their ground states.

The excess energy is zero for pure clusters by definition. Negative excess energies indicate that the formation of the corresponding nanoalloy is energetically favourable, as compared to an ideal mixture.

We also determined the second difference in energy of the nanoalloys to analyse their relative stabilities from another point of view:

$$\Delta_2 E(x) = E(x+1) + E(x-1) - 2 \times E(x) \quad (2)$$

where $E(x)$ is the correspondent energy of the nanoalloy, and $E(x\pm1)$ is the energy of neighbouring stoichiometry. x stands for the number of atoms in Fe_xNi_{13-x}.

A maximum in the second difference in energy allows us to know how much stable is a nanoalloy with respect to neighbouring stoichiometries. Thus, $\Delta_2 E(x)$ is an indicator for the most abundant composition.

In order to provide information about the stability of both atomic and molecular oxygen adsorption sites, we define the absorption energy as

$$E_{molecular} = E_b + E_{O_2} - E_a \quad ; \quad E_{atomic} = E_b + 2E_O - E_a \quad (3)$$

where E_a (E_b) is the energy of the cluster after (before) oxidation. E_{O_2} (E_O) is the energy of the oxygen molecule (atom).

As the absorption energy value increases, the oxygen is more bounded to the cluster, and thus the adsorption site is more stable.

B. Global reactivity indicators

In order to characterize the global reactivity of our Fe_xNi_{13-x} nanoalloys, we have modified the total charge of the structure adding or removing an electron, and then submitted electronic relaxations to our neutral structures. This allowed us to calculate conceptual DFT based quantities[25], such as the vertical ionization potential I and the vertical electron affinity A:

$$I = E(N-1) - E(N) \quad ; \quad A = E(N) - E(N+1) \quad (4)$$

where N is the number of electrons of the neutral clusters and the energies are calculated for the atomic structures of the neutral nanoalloys after relaxing only the electronic part. By the definitions of I and A we can mathematically define our global reactivity descriptors[26], firstly, the electronegativity[27] (the negative of the electronic chemical potential μ):

$$\chi = -\mu = -\left(\frac{\partial E}{\partial N}\right)_{\nu} = \frac{1}{2}(I + A) \quad (5)$$

and then the chemical hardness η, also defined as half the fundamental GAP (E_{gap}):

$$\eta = \frac{1}{2}E_{gap} = -\left(\frac{\partial^2 E}{\partial N^2}\right)_{\nu} = \frac{1}{2}(I - A) \quad (6)$$

An electrophilicity index[28] can be defined as:

$$\omega = \frac{\chi^2}{2\eta} = \frac{\chi^2}{E_{gap}} \quad (7)$$

C. Local reactivity indicators

Since most of the chemical reactions involve some change in the electron density of the molecules, we needed a way to determine this change and to study its role in the reactivity of the molecules. Fukui functions[29,30,31], f^+ and f^-, describe local variation in electron density of a system at a given position when the number of electrons is changed, and thus, allow to predict plausible reactive sites according to purely electronic arguments.

The Fukui functions are defined as follows:

$$f^{\pm}(\vec{r}) = \left(\frac{\partial \rho(\vec{r})}{\partial N_e}\right)^{\pm}_{\nu} \tag{8}$$

where $\rho(\vec{r})$ is the spatial charge density, N_e is the number of electrons, and the subscript ν indicates that the partial derivatives must be calculated at a constant external potential. This implies that the atomic coordinates have to be fixed.

This mathematical definition allows us to understand the Fukui functions $f^{\pm}$ as scalar fields that measure local variations in the electronic charge caused by the addition or removal of electrons. Because of this, they can be used as local indexes of electronic reactivity. Superscript '+' refers to the electron density variation with the addition of electrons, and it indicates locally electrophilic regions, sensitive to nucleophilic reactions. And superscript '-' alludes to electron density variation with the removal of an electron, designating the locally nucleophilic regions, susceptible to electrophilic reactions.

Bader analysis allows to determine the variation in electronic charge inside the Bader atomic volumes, defining an atom-condensed Fukui function or condensed reactivity indicator $f_i^{\pm}$ for any atom 'i' in the cluster. This atom-condensed function approximates the derivatives by finite differences in the electronic charge. The form of the function depends on whether we add or remove an electron from the molecule.

The condensed Fukui function for the addition of an electron to a molecule is:

$$f^+_{Ne}(\vec{r}) = \rho_{Ne+1}(\vec{r}) - \rho_{Ne}(\vec{r}) \tag{9}$$

And for the removal of an electron:

$$f^-_{Ne}(\vec{r}) = \rho_{Ne}(\vec{r}) - \rho_{Ne-1}(\vec{r}) \tag{10}$$

This involves converging the electronic structure of both cation and anion at the optimal neutral geometry in all our concentration range. However, when we make a calculation of a charged system with a certain number of electrons, the energy converges very slowly. This can be dealt with the addition of a Madelung correction. We have applied the necessary corrections (dipole corrections included) to properly obtain the total energy of the cluster. Although the finite difference expressions provide the exact value for the derivative according to DFT[32], in practical calculations the expressions are not exact. This is because of the self-interaction error of approximate exchange-correlation functionals. Nevertheless, the standard use of those finite difference instead of the partial derivatives is justified by the fact that the approximations made in exchange-correlation functionals are much more accurate for integer numbers than for fractional numbers of electrons.

III. RESULTS

The selected trial structures used for our calculations (those of the neutral nanoalloys) can be seen in Figures A1 to A3 of the Supplementary Information (figures referring to the SI will always be marked with an A before the corresponding number). In many images we will use the following code; first (second) number under the structure indicates the number of iron (nickel) atoms. Roman numbers indicate stability, 'I' stands for the ground state, and 'II', 'III' and 'IV' are the first three isomers in order of stability. Under this numbers, the energy difference with respect to that of the ground state (in eV), and magnetic moment (in μ_B) are given. Iron (Nickel) atoms will be represented in orange (green).

A. Structural Properties and Stability

Using as input the structures obtained in our previous work[12], we calculated the cationic and anionic clusters by removing and adding an electron to the structure respectively. The neutral and charged $Fe_xNi^{0/\pm}_{13-x}$ nanoalloys are summarized in Figs. A1 to A9 of the Supplementary Information, both the ground state and the first three structural isomers. In order to compare the difference between Ground State (GS) structures for the three states of charge, we collect these GS in Figs. 1 to 3. Pure nickel and iron neutral clusters are presented in Fig. A10.

As we can see in Figs. 1 to 3, in most concentrations the neutral GS structure is preserved for the two charged states. Only charged clusters with a small number of iron atoms present a different structure from the one ex-

hibited by the neutral cluster ($Fe_2Ni_{11}^-$, $Fe_4Ni_{10}^-$ and $Fe_4Ni_9^+$). Although the structure does not change, some charged stoichiometries exhibit a different GS homotop than that of the neutral state. These other stoichiometries are $Fe_6Ni_7^-$, $Fe_9Ni_4^-$, $Fe_{10}Ni_3^+$ and $Fe_{11}Ni_2^\pm$. Different homotops correspond to different chemical orders, or, in other words, different relative positions of the two constituents within the atomic skeleton

Ni-rich zone (see Fig. 1) presents a great variety in structures, even more, in this zone appear all the cases of structural change with the state of charge. However, no homotop change take place in this zone. While the cation has the same structure as the neutral system at $x = 1, 2, 3$, the anion shows a decahedral structure as GS since Fe_2Ni_{11}. Anionic an neutral ground states match again at Fe_4Ni_9, were the neutral state first present a decahedral GS, while an icosahedral structure is preferred by the cationic state.

For the equiatomic regime ($x = 5-8$, see Fig. 2), solely decahedral structures are obtained. Only one change in the GS homotop is observed in this zone ($Fe_6Ni_7^-$), different from its neutral and cationic counterparts. This makes the equiatomic zone robust against changes in Fe-Ni concentration and net charge. The disposition of Ni atoms in the corners and external sites of the decahedral structures maximizes the number of Fe-Fe bonds.

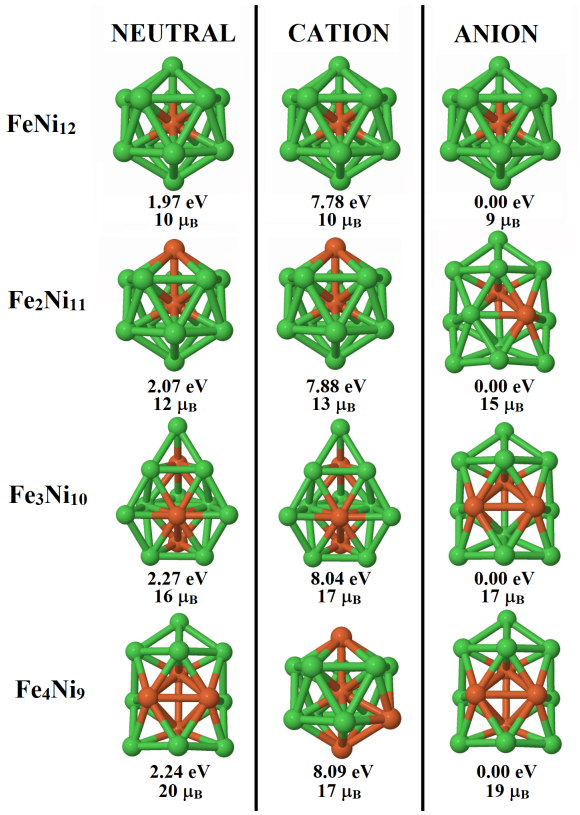

FIGURE 1: Comparison between the neutral, cationic and anionic Fe_xNi_{13-x} GS structures in the $1 \leq x \leq 4$ cluster range. Below each nanoalloy is given the cluster difference in energy with the most stable state of charge, as well as the total spin magnetic moment.

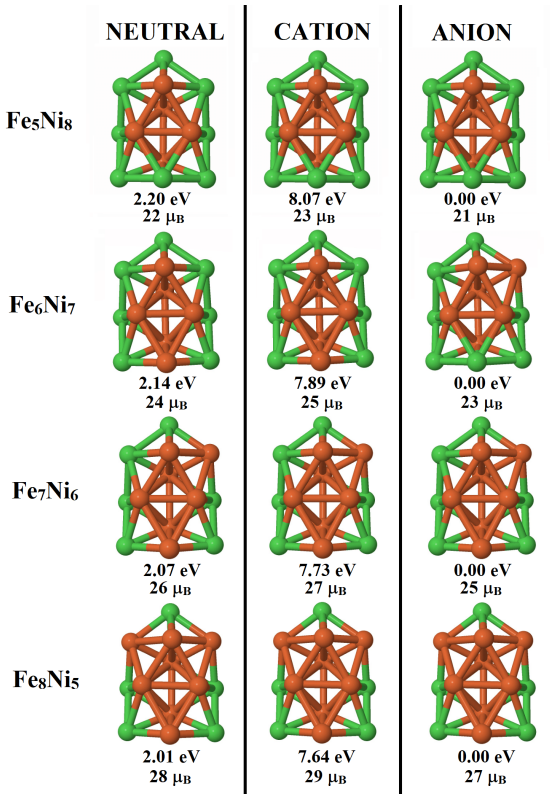

FIGURE 2: Comparison between the neutral, cationic and anionic Fe_xNi_{13-x} GS structures in the $5 \leq x \leq 8$ cluster range. Rest of the caption is the same as in the previous figure.

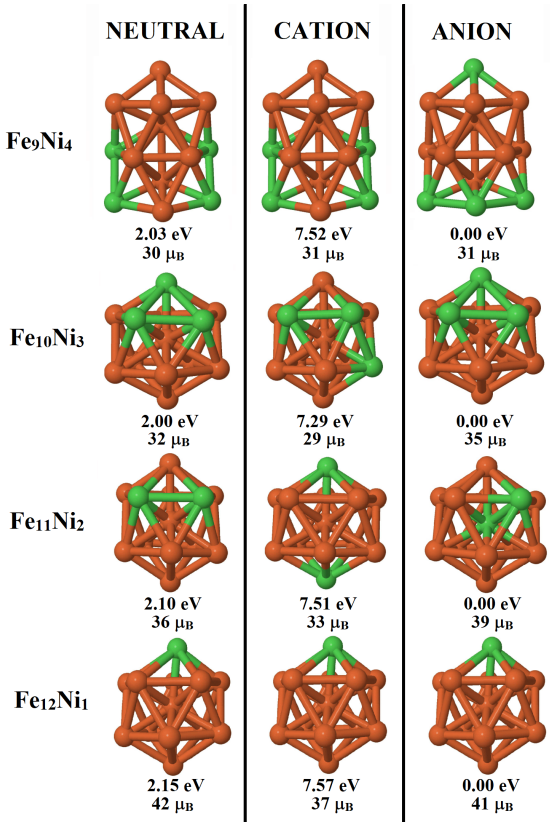

FIGURE 3: Comparison between the neutral, cationic and anionic Fe_xNi_{13-x} GS structures in the $9 \leq x \leq 12$ cluster range. Rest of the caption is the same as in the previous figure.

The Fe-rich zone (see Fig. 3) is dominated by icosahedral structures, and in less concentration (only at Fe_9Ni_4), decahedral structures. This zone does not present changes in the cluster structures upon ionization or e^- excess. However, is in this zone where most changes of GS homotop changes take place with an e^- deficit or excess. The $Fe_{11}Ni_2$ stoichiometry is the only one in all our concentration range which has a diferent homotop for each state of charge. In both Ni and Fe-rich regions, almost all the icosahedral structures present an iron atom as its central site. The only exception is $Fe_{11}Ni_2^-$, which is the second excited isomer of the neutral cluster.

Now we move onto the stability analysis, where we study the excess and second difference in energy of the clusters. The excess energies (Fig.2, a) of both charged states are negative in ten of the eleven nanoalloys, indicating that their formation from the pure iron and nickel clusters is an exothermic process. The only exception is the $Fe_{12}Ni^{0/-}$ GS structure, which shows a positive excess energy. We can see that this composition shows a minimum in the second difference in energy (Fig.2, b), making it less stable than its neighbours.

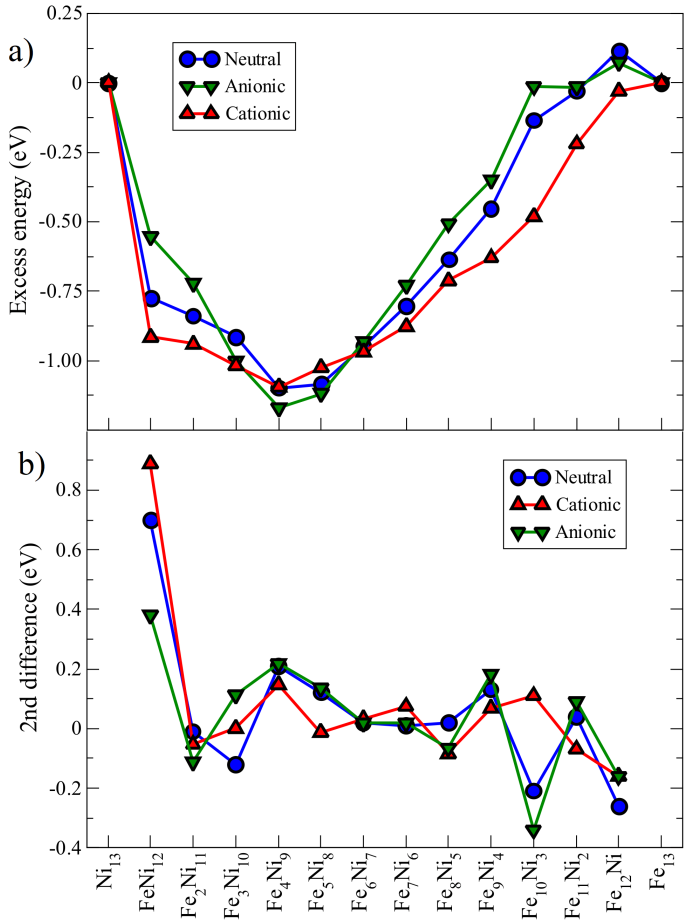

FIGURE 4: Excess energy (a) and second energy difference (b) in eV, of charged $Fe_xNi^{\pm}_{13-x}$ nanoalloys.

Charged Fe_xNi_{13-x} nanoalloys with $x = 3-7$ are clearly more stable than the rest, and the three states of charge find their minimum excess energy at Fe_4Ni_9 (magic composition), where the charged states exhibit different structures. This compositions also shows a local maxima for every state of charge, indicating its relative stability with respect to its neighbours. Nevertheless, it is important to notice how the majority of the compositions presenting a low excess energy value (between $x = 3-6$) are decahedral geometries, except for one pyramidal ($Fe_3Ni_{10}^+$) an one icosahedral structure ($Fe_4Ni_9^+$). This hints the structural dependence of the cluster stability, pointing the decahedral structure as the most stable in this composition range. The most stable geometries are the decahedra that have their corner sites filled with nickel atoms, with smaller pure iron subclusters in their inside.

Some differences can be seen between the two limits of our concentration range. Towards the Ni-rich phase the excess energy decreases fast because of the sudden changes in the cation and anion geometries. Near the Fe-rich zone, the anion clusters excess energy shows a value near zero (the same as a pure cluster). Meanwhile, the cations' excess energies decrease faster, this can be explained by the smaller coordination between Ni-atoms in the cationic nanoalloys with respect to the anionic ones.

Analyzing the second energy difference, the three states of charge share two maxima at $FeNi_{12}$, where all states share the same icosahedral GS structure, and at the magic composition (Fe_4Ni_9), which is the most stable. The next two maxima for the anion are the Fe_9Ni_4 (decahedron) and $Fe_{11}Ni_2$ (icosahedron) compositions, while the cation presents maxima for Fe_7Ni_6 (decahedron) and $Fe_{10}Ni_3$ (icosahedron). Both charged systems present minima at Fe_2Ni_{11}, Fe_8Ni_5, which do not coincide with the local minima of the neutral system. However, the anion shares minimum with the neutral state at $Fe_{10}Ni_3$, where both have the same structure, while the cation presents the above mentioned maximum. The cation also shows another different local minimum at Fe_5Ni_8, which is its first decahedral GS structure. The three states of charge have a matching minimum at $Fe_{12}Ni$.

To sum up, the change in electrical charge triggers local second energy difference maxima at different compositions. Decahedral structures with nickel atoms in their external and corner positions have the lower excess energies, thus being the most stable. The magic composition presents a local second energy maxima for the three states despite them having different structures, hinting the importance of the nanoalloys' composition, and making the Fe_4Ni_9 structure more stable than its neighbouring stoichiometries.

B. Electronic and Magnetic Properties

In this section we discuss the electronic and magnetic properties of $Fe_xNi_{13-x}^{0/\pm}$ nanoalloys. In Fig. 5 the magnetic moments of the three states of charge of the Fe_xNi_{13-x} nanoalloys are presented. As the number of iron atoms increase, the magnetic moment of the nanoalloy also increases. This holds for all states of charge, being consistent with the fact that the iron atom has a $2.2\mu_B$ magnetic moment in its bcc bulk, while the nickel atom has a $0.6\mu_B$ magnetic moment in its fcc bulk. The same trend is also seen in isolated atoms based on Hund's rule. However, the result is not obvious, since Fe exhibits antiparallel couplings in Fe_{13}^+, which was studied by Vega et al[33]. In many cases, the magnetic behaviour of the charged nanoalloys does not exhibit the $\pm 1\mu_B$ difference with the neutral state magnetic moment. Most of exceptions that show a bigger change in magnetic moment present a GS structural or homotopic change with respect to the neutral cluster. For example, in the Ni-rich zone, $Fe_2Ni_{11}^-$ and $Fe_4Ni_9^+$ present a $+3\mu_B$ and $-3\mu_B$ difference with the neutral cluster respectively. This is due to the fact that their GS structure is different from the GS of the neutral state.

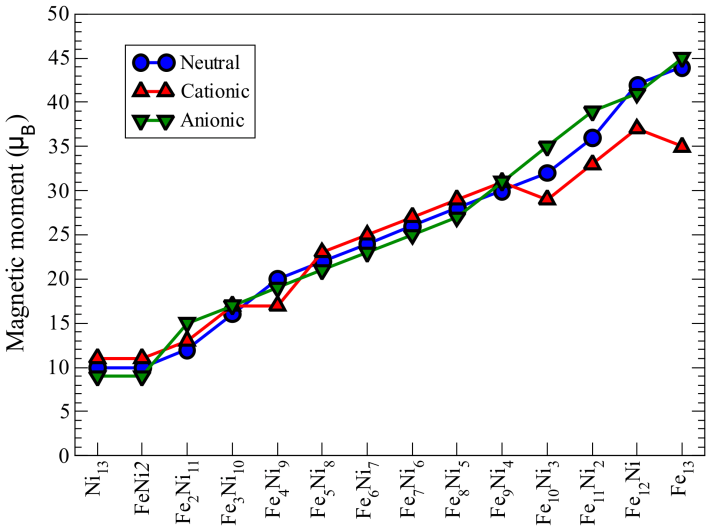

FIGURE 5: Magnetic moment of the neutral (blue), cationic (red) and anionic (green) GS structures od the Fe_xNi_{13-x} nanoalloys.

When looking at the Fe-rich zone, a similar analysis can be made. Due to their GS homotopic changes with respect to the neutral cluster, $Fe_{10}Ni_3^+$ and $Fe_{11}Ni_2^\pm$ show a magnetic moment difference of $-3\mu_B$ and $\mp 3\mu_B$ respectively. Nevertheless, other compositions such as $Fe_{10}Ni_3^-$, $Fe_{12}Ni_2^+$ and Fe_{13}^+ present a big magnetic moment change without an structural or homotopic change in their GS. For example, Fe_{13}^+ shows a great difference $(-9\mu_B)$ with the neutral state magnetic moment due to an antiparallel coupling of the central atom[33]. The expected magnetic behaviour of the nanoalloys can be observed towards the equiatomic composition, where the cation (anion) has $1\mu_B$ more ($1\mu_B$ less) than the neutral system. This is expected due to the fact that in most compositions, the three states of charge have the same or similar decahedral GS structure.

C. Reactivity

The electronegativity quantifies the ability of nanoalloys to attract and hold electrons. The results in Fig. 7 (a) shows the GS structures' electronegativity values of each composition, but no systematic trend is to be found. This is due to the fact that the ground state structure is not the same across the composition range, showing a perfect non-scalability example of the nanoscale. The electronegativity greatest value is exhibited by the pure nickel cluster, and immediately decreases as we increase the number of iron atoms while maintaining the icosahedral structure. However, the electronegativity shows a sudden local maximum at Fe_5Ni_8, and a similar value for the magic composition (Fe_4Ni_9). As we have studied, both compositions showed the same decahedral structures in the neutral and anion states, exhibiting great stability. In both compositions of this geometry, the nickel atoms are located at the external positions of the cluster, minimizing the nickel atomic coordination and creating smaller pure iron subclusters inside of the nanoalloys. As the iron starts to fill the external sites of our decahedral structures (at Fe_6Ni_7), the electronegativity decreases until it reaches a global minimum at $Fe_{10}Ni_3$, the first icosahedral structure after the equiatomic region.

The chemical hardness quantifies the sensitivity of the chemical potential (negative electronegativity) to changes in the number of electrons. The larger the hardness, the more reluctant the material to accept or donate electrons. Chemical softness (inverse of the hardness) correlates with the system polarizability. As it can be seen in Fig. 7 (b), chemical hardness and electronegativity resemble each other but show some important differences. Despite having one of the highest electronegativity values, the magic composition $Fe_{10}Ni_3$ presents a local chemical hardness maximum, therefore it is less reactive (not willing to change its number of electrons). Meanwhile, Fe_5Ni_8 shows a local minimum in chemical hardness, because of this, not only has the highest electronegativity of the nanoalloys, but also favours a change in its number of electrons (compared to its neighbours). Our minimum in electronegativity ($Fe_{10}Ni_3$) is also the chemical hardness minimum, showing that despite not having a great ability of attracting and holding electrons, it is willing to change its number of electrons.

The electrophilicity index measures the energy change of a system upon maximum uptake of electrons, this is until the electronegativity vanishes. It is related to the electron affinity, that measures the energy change after adding one electron. In fact, based on the definition of ω, its composition dependence matches exactly the one of the affinity A. In Fig. 7 (c) we can see that the electrophilicity index presents a lot of variation, as it has two

major minima at $FeNi_{12}$ and $Fe_{10}Ni_3$ and one global maximum at Fe_5Ni_8, that also showed the electronegativity maximum. With the exception of $Fe_{10}Ni_3$, which is the global minimum of the three global reactivity indicators, the lower values correspond to high values of chemical hardness. This implies that nanoalloy icosahedra with few iron atoms, pyramids, and decahedra with many iron atoms present higher electronic stability. Meanwhile, near the pure iron limit, where all the geometries are icosahedrons, ω shows an increasing value with the number of Fe atoms. A similar analysis can be made for the decahedral structures close to the magic composition.

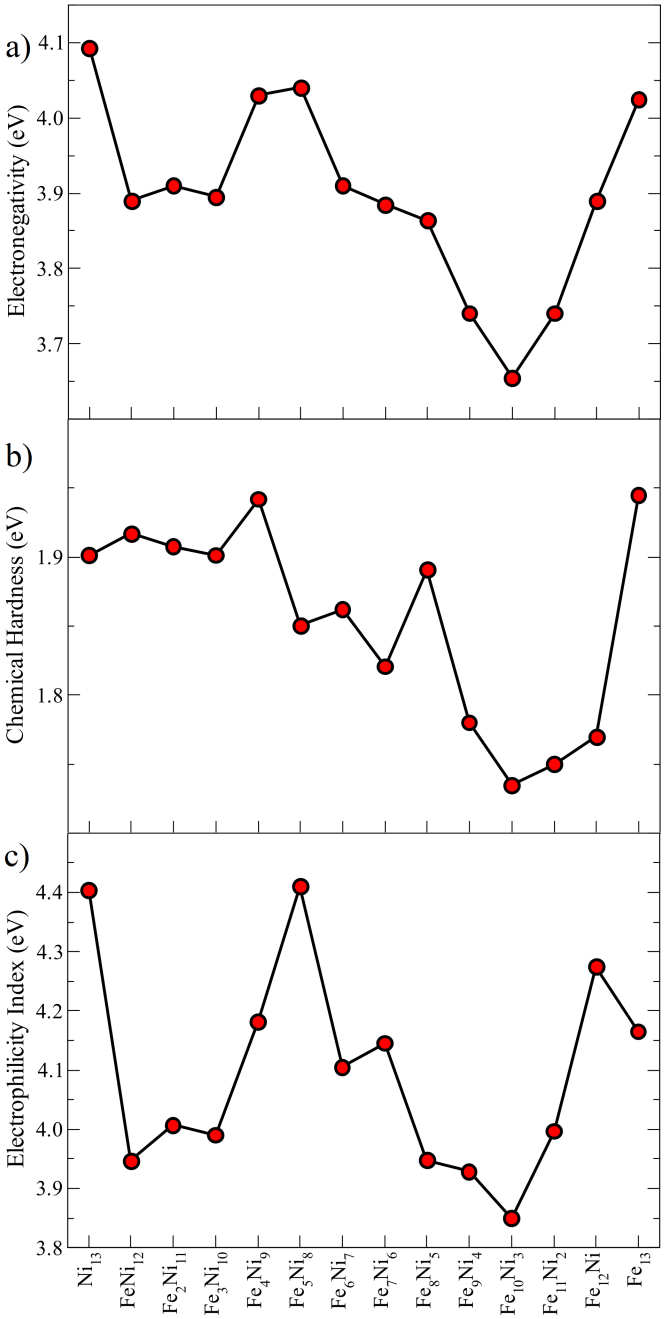

FIGURE 7: Global reactivity indicators. Electronegativity (a), chemical hardness (b) and electrophilicty index (c) of the $Fe_xNi^{\pm}_{13-x}$ nanoalloys.

Now we turn to an analysis of local reactivity descriptors. The previously defined atom-condensed Fukui functions provide a local resolution in space of the global trends just discussed. A visual colour trend of values of both Fukui functions f^+ and f^- are plotted in Figs. 8 and 9 respectively. The f^+ function shows the local electrophilic character of the nanoalloy, and is appropiate to understand the initial stage of a nucleophilic attack. On the other hand, the f^- function identifies the locally nucleophilic regions of the nanoalloy, providing information about the initial stages of an electrophilic attack. In both cases, higher values of the Fukui function identify chemically softer local regions.

Fig. 8 offers an easy visualization of the electrophilic Fukui function f^+ values on every atomic site. Giving us information about which sites would be preferentially attacked by an electron donor perturbation, like solvated anions. As happened with global reactivity descriptors, Fukui functions are geometry-dependant because of the ground states not being the same in all our composition range. However, several conclusions can be extracted from the figure: (i) The smaller the atomic coordination, the higher f^+ value, regardless of the atom species. (ii) In the Ni-rich and equiatomic zones ($x = 1 - 8$), the maximum values of f^+ are generally located at nickel atoms, with the exception of the iron atom at Fe_2Ni_{11}, which is symmetrically opposed to the nickel atom with the maximum f^+ value, and has a bigger f^+ value than the rest of nickel atoms. (iii) Towards the Fe-rich zone ($x = 9{-}12$), iron atoms present the higher f^+ values. (iv) Icosahedral structures show the minimum value of f^+ at their central atom, which is always an iron atom. This suggests that the incoming electrons will be absorbed and distributed all over the surface of the icosahedron. This is clearly seen at $FeNi_{12}$, where all the surface is formed by nickel atoms that have the same f^+ value. (v) Pyramidal and decahedral structures present the maximum value of f^+ at the top and corner sites of the structure, where always lays a nickel atom until Fe_9Ni_4, where an iron atom stands in the top of the structure, exhibiting the maximum f^+ value. (vi) The iron atoms at the central sites of the pyramidal and decahedral structures exhibit the lower f^+ values.

In Fig. 9 we provide a similar analysis of the nucleophilic Fukui function (f^-), that identifies atomic sites preferentially attacked by electron acceptor perturbations such as an oxygen rich environment. This is particularly interesting because, as we have previously said in Section I, FeNi nanoalloys show a relevant potential of becoming good electrocatalyst for water splitting. This reaction should be produced by the oxidation of our nanoalloy, breaking the water molecule and thus releasing the hydrogen. Similar trends and conclusions as the ones extracted from the f^+ can be seen for f^-. (i) As atomic coordination decreases, the nucleophilic Fukui function increases. However, f^- presents higher values at nickel

atoms than it does for iron atoms, even when the latest appear in decahedral top positions, thus having a more marked atom species-dependence than f^+. (ii) Nickel atoms show the higher f^- value for $x = 1-9$ structures, with the same exception as the one f^+ presented. (iii) Fe atoms exhibit the highest f^- values since $Fe_{10}Ni_3$. However, nickel atoms do not present the smaller f^- values, but similar values as the iron ones (except for $Fe_{11}Ni_2$). This is the main difference with f^+, where nickel atoms showed the smaller values in this zone. (iv) As well as for f^+, the icosahedral structures present the smallest f^- value at the central iron atom. (v) Nickel atoms at the top and corner sites of pyramidal and decahedral structures have the higher f^- values. (vi) Iron atoms at the centre of these structres present the lower values of f^-.

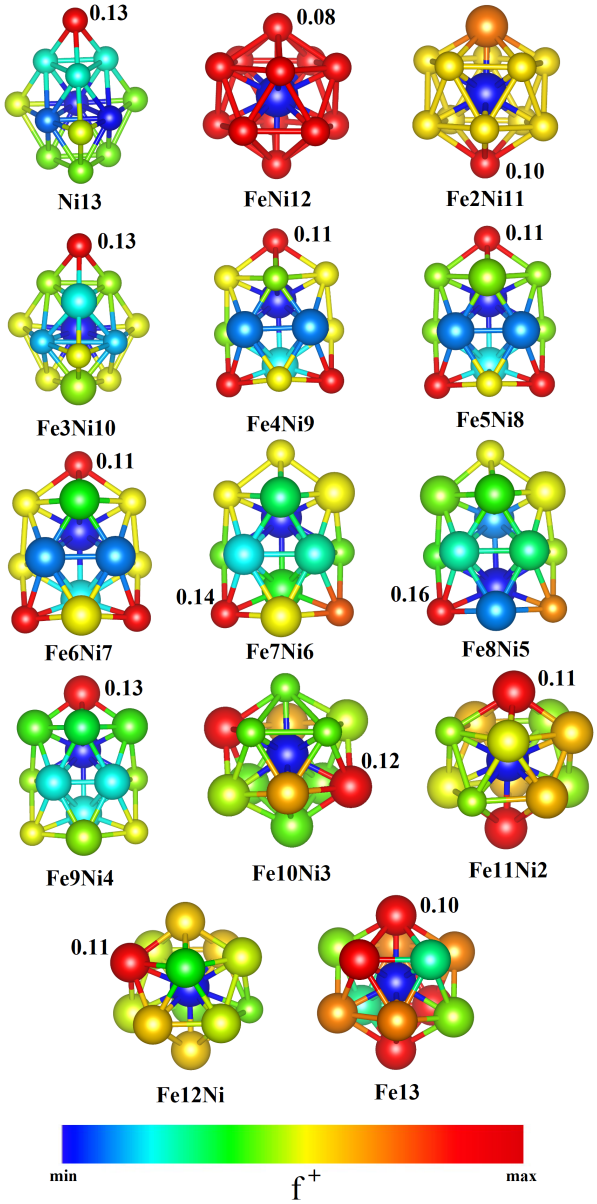

FIGURE 8: Electrophilic Fukui function f^+ of the Fe_xNi_{13-x} GS structures. Small spheres represent Ni atoms, large spheres represent Fe atoms. The colour of the atoms designates the value of the fukui function as indicated in the figure legend. The maximum value of f^+ is explicitly annotated next to the corresponding atom.

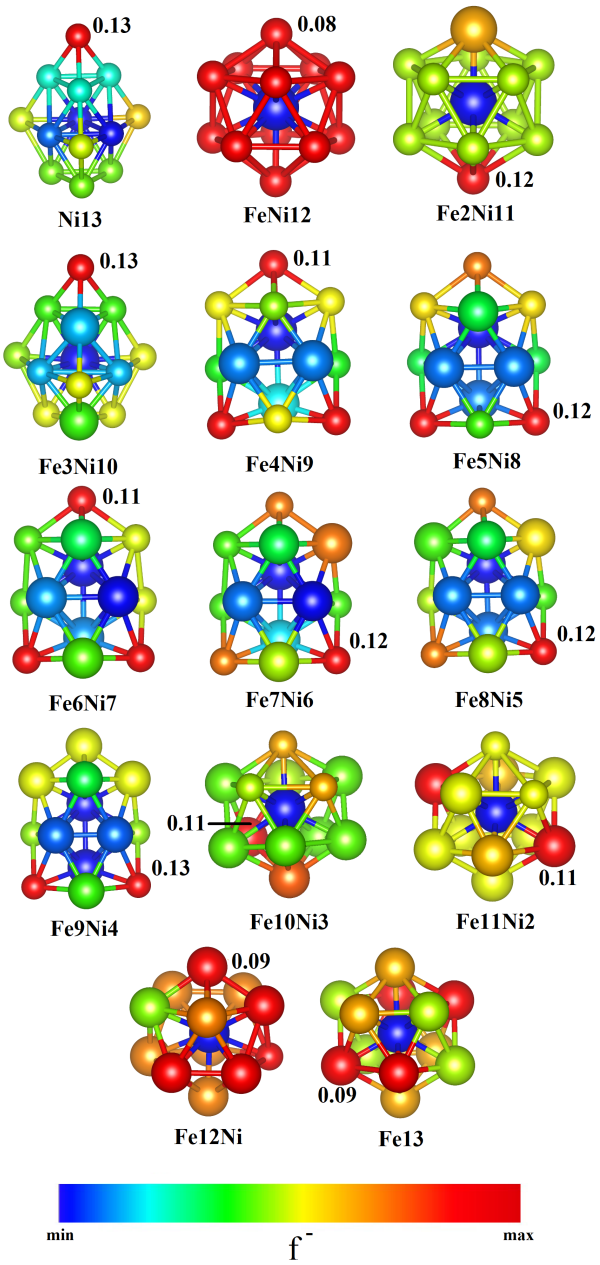

FIGURE 9: Nucleophilic Fukui function f^- of Fe_xNi_{13-x} GS structures. Rest of the caption is the same as in the previous figure.

Fig. 10 displays the average values of the two Fukui functions on Fe and Ni atoms. One can see that iron atoms have, on average, smaller values than nickel atoms for both Fukui functions. Both maximum f^+ and f^- values can be located at nickel sites of Fe_8Ni_4 and Fe_9Ni_4 respectively, while the minimum value of both functions can be seen at the iron atom of $FeNi_{12}$. This correlates with the fact that this atom stands in the centre of the icosahedral structure, sharing its charge with the surrounding nickel atoms (as we have seen in the Bader charge analysis). f^+ and f^- exhibit a local minimum at the iron sites of the magic composition, which is the most stable structure. It is an interesting conclusion that, generally, Ni sites are on average the most reactive

ones towards both reducing and oxidizing agents. We believe that this finding is directly related to the preferential occupation of corner sites (which are the most reactive ones) by nickel atoms across most of the composition range. Nickel f^- values do not decrease when iron atoms occupy decahedral corner sites, and only presents one value where iron atoms have higher value than nickel ones ($Fe_{11}Ni_2$), even when they occupy equivalent positions. This proves the f^- atom species-dependence, which shows, even in the Fe-rich zone, higher values at nickel atoms.

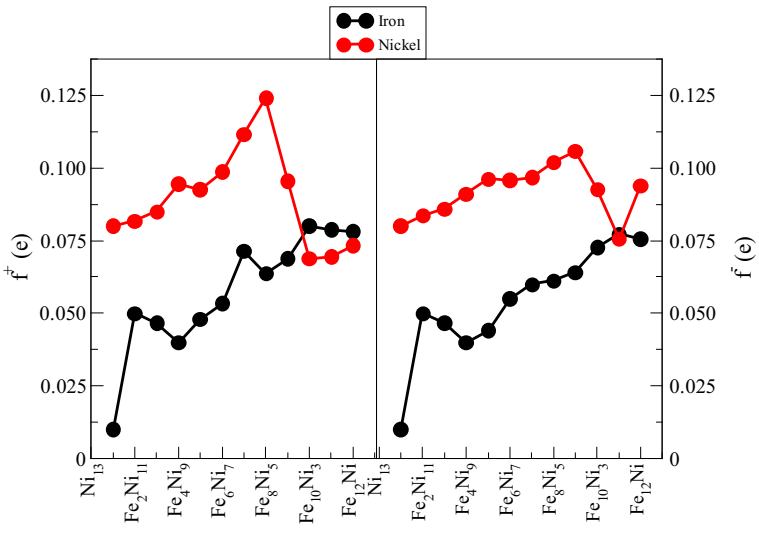

FIGURE 10: Composition dependence of the average atom-condensed Fukui function values for Fe atoms (black curves) and Ni atoms (red curves). f+ and f- results are shown on the left and right panels respectively.

D. Oxidation

Finally, several calculations of oxygen adsorption were conducted for three of our compositions. We present results obtained for two decahedral structures: Fe_4Ni_9 and Fe_5Ni_8, which presented the maximum electronegativity among the different compositions. Besides, calculations are also made for the $Fe_{10}Ni_3$ icosahedron, that exhibited the minimum chemical hardness, electronegativity and electrophilicity index values. All non-equivalent positions of the cluster, bridge, hollow and top sites, are tested with different molecular oxygen adsorption. Furthermore, calculations for dissociated oxygen are also conducted in order to fully characterize the first stage of oxygen adsorption.

In the magic composition (Fig. A11), we can see how the most stable clusters are the ones showing dissociated oxygen adsorption. The preferred positions for the atomic oxygen adsorption are hollow sites near the corners of the structures, as we can see in both the ground state configuration and first isomer, as well as in other structures of the first twelve isomers. This was expected because the external and corner sites displayed highest values of f^-. Nonetheless, in less stable isomers one oxygen atom stands in a corner position, and the other lays in the central site of the decahedron, hinting the importance of the structure's symmetry. The most stable O_2 adsorption site is the bridge position, showing its most stable geometry when the bridge site corresponds to a Ni-Ni or Fe-Ni bond. In fact, whenever the bridge site stood over a Fe-Fe bond in the initial structure, it dissociated after the relaxation. Lastly, the top and hollow O_2 adsorption site geometries appear as the least stable configurations. Few O_2 hollow adsorption sites appear due to the fact that most of them have relaxed into dissociated O adsorption sites. A similar analysis can be made for the $x = 5$ dechaedron (Fig. A12), with the main difference being the most stable bridge O_2 adsorption site, that stands over a Fe-Fe bond.

Moving onto the $Fe_{10}Ni_3$ icosahedron (Fig. A13), several conclusions can be drawn. As what we found in Fe_4Ni_9, Fe_5Ni_8 decahedral structures, dissociated oxygen adsorption is the most stable of the adsorption processes. The preferred positions for the oxygen atoms are the hollow sites close to the iron atoms with higher f^- values. However, in less stable isomers, an oxygen atom also lays on hollow positions near the nickel atoms that also exhibited high f^- value. The most stable molecular oxygen adsorption is the bridge site when standing over Fe-Fe bonds, while the least stable ones are on the Fe-Ni bonds. The main difference is seen in the hollow adsorption sites, which remain the same after relaxation, proving to be far more stable than in the decahedral structures.

In Fig. 11 we present the best three atomic and molecular oxygen adsorption sites, as well as their oxygen absorption energies. It is noticeable that, in the three stoichiometries, atomic adsorption is more stable than molecular adsorption, with a difference of $\sim 10eV$. While the two decahedral structures show similar oxygen absorption energies, both atomic and molecular, $Fe_{10}Ni_3$ presents higher energy absorption values, exhibiting a difference of $\sim 1.25eV$ ($\sim 0.71eV$) for O_2 (O) with Fe_4Ni_9, Fe_5Ni_8. This means that $Fe_{10}Ni_3$ presents far more stable adsorption sites, for both atomic and molecular oxygen adsorption. This can be explained by the fact that $Fe_{10}Ni_3$ is the global chemical hardness minimum, thus being the most reactive. Besides, it has the lowest electronegativity so that it is more prone to donate e^- to oxygen.

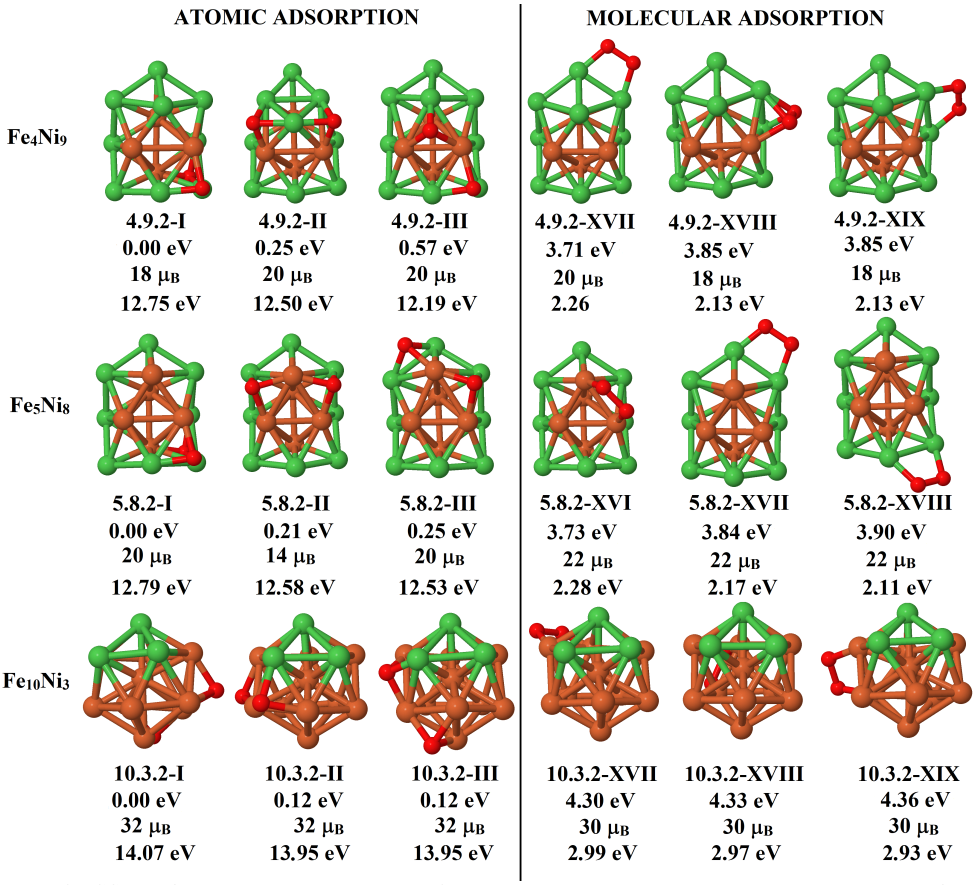

FIGURE 11: $Fe_xNi_{13-x}O_2$ GS and first two structural isomers of both atomic and molecular oxygen adsorption. The first number indicates energy difference with the ground state, second number is the magnetic moment, and last number shows the absorption energy, as defined in Section II.

IV. SUMMARY AND CONCLUSIONS

Ab initio DFT calculations in the generalized gradient approximation to exchange and correlation were conducted for $Fe_xNi^{\pm}_{13-x}$ nanoalloys in all the composition range with the aim of obtaining, from a first principles perspective, a better understanding of the potential of Fe-Ni nanoalloys as catalysts for certain reactions. In this paper we provide information about the reactivity of these nanoalloys and the first stages of their oxidation. Putative global minimum geometries of the charged nanoalloys were found by relaxing the neutral ground state structures and the first three structural isomers after changing the number of electrons. Local electronic charges were evaluated using Bader's method, as well as their magnetic moment. Global and local reactivity descriptors were also calculated. Among the global ones, we determined the vertical ionization potential, vertical electron affinity, electronegativity and chemical hardness. Among the local ones, we calculated the atom-condensed Fukui functions.

Low energy structures of charged nanoalloys were described by two attributes: ionic skeleton and stoichiometry, and then compared to their neutral counterparts. We found that, generally, the state of charge does not change the GS geometry, but some compositions presented a different charged structure from the neutral system in the Ni-rich zone, and towards the Fe-rich zone, a few clusters exhibited a different homotop from the neutral state, proving that the addition or removal of an electron can affect the GS structure. To locate the most stable nanoalloys, an study of their excess and second energy difference was performed. We found that the formation of almost all nanoalloys is an exothermic process. The global excess energy minimum can be seen at Fe_4Ni_9, which also shows a local second energy difference maximum. Although the anionic local second energy difference maxima matched neutral maxima, the change in electrical charge triggered local maxima at different compositions for the cationic state. However, the local maximum at the magic composition (Fe_4Ni_9) remains for all states of charge.

Analyzing the magnetic moment of the clusters, a global trend can be observed: as the number of iron atoms increases, so does the total magnetic moment of the cluster. However, the expected behaviour of $\pm 1\mu_B$ for the charged nanoalloys is only found close to the

equiatomic region, were all three states of charge share the same or similar decahedral structure. This is not the case in the Ni- and Fe- rich zones, where the charged GS structural or homotopic changes result in a larger magnetic moment difference with the neutral states. Mostly parallel couplings are observed, with the one exception of Fe_{13}^{+}[33], which exhibits an antiparallel coupling in its central atom. Applying Bader's method, it was concluded that a charge transfer from iron to nickel atoms always occurs (Fig. A14), even in low nickel concentration stoichiometries, and that the Bader charge value on an specific atom is triggered by the number of Fe-Ni bonds.

Regarding the reactivity, no trend was found in the global reactivity descriptors as a function of the composition. This is due to the great variety of GS structures across the composition range. The change in geometry fits the changes in the slope of the electronegativity, for instance. However, there were some sudden electronegativity maxima at the magic composition (Fe_4Ni_9) and Fe_5Ni_8, decahedral structures with nickel atoms on their corner sites. These structures showed to be the maximum chemical hardness and electrophilicity index values, respectively. One global minimum was found in all global reactivity descriptors at $Fe_{10}Ni_3$, the first icosahedral structure after the equiatomic zone. The electrophilic Fukui function presented its highest values at the corner sites of pyramidal and dechaedral structures, showing minimum values at the central iron atoms. Icosahedral structures present the lowest f^+ value at the central iron atom, and the higher values at nickel (iron) atoms in the Ni-rich (Fe-rich) zone. Similar results are obtained for the nucleophilic function. However, f^- exhibits an atomic species dependence, that f^+ did not, showing higher values at nickel atoms, even when iron atoms occupy the corner (and thus, more reactive) sites. On average, Ni sites are more reactive towards reducing and oxidizing agents, due to their preferential position of corner sites across the majority of the composition range.

Dissociated oxygen adsorption is the most stable process for the three compositions studied ($Fe_4Ni_9, Fe_5Ni_8, Fe_{10}Ni_3$). In both decahedral structures ($x = 4, 5$) the oxygen atoms prefer to stand near the corner sites, where the iron-nickel charge transfer favours the oxygen adsorption, as predicted by this positions' high f^- values. The most stable O_2 adsorption is at the bridge sites. These do not appear near high f^- values at the GS, but do on the most stable structural isomers. Most O_2 hollow adsorption sites relax into dissociated O for the decahedra, and only remain undistorted for $Fe_{10}Ni_3$. Lastly, the O_2 top adsorption sites seem to be the least stable for every composition. An analysis of the absorption energy revealed that, of the three studied nanoalloys, the global chemical hardness and electronegativity minima ($Fe_{10}Ni_3$), presents the most stable adsorption sites, both atomic and molecular.

V. REFERENCES

[1] A. Aguado, Chapter 3 Modeling the electronic and geometric structure of nanoalloys, Nanoalloys From Fundamentals to Emergent Applications, 75-111 (2013).
[2] C. Lee, D. Sedlak, Enhanced Formation of Oxidants from Bimetallic Nickel-Iron Nanoparticles in the Presence of Oxygen, Environ. Sci. Technol. 42, 8528 (2008).
[3] C. Park, N. M. Rodriguez, R. T. K. Baker, Carbon Deposition on Iron–Nickel during Interaction with Carbon Monoxide–Hydrogen Mixtures, Journal of Catalysis 169, 212–227 (1997).
[4] C. Park, R. T. K. Baker, Carbon Deposition on Iron–Nickel during Interaction with Ethylene–Hydrogen Mixtures, Journal of Catalysis 179, 361–374 (1998).
[5] X. Long, G. Li, Z. Wang, H. Zhu, T. Zhang, S. Xiao, W. Guo, S. Yang, Metallic Iron-Nickel Sulfide Ultrathin Nanosheets As a Highly Active Electrocatalyst for Hydrogen Evolution Reaction in Acidic Media, J. Am. Chem. Soc. 137, 37, 11900-11903 (2015).
[6] Y.Wang, C. Xie, D. Liu, X. Huang, J. Huo, S. Wang, Nanoparticle-Stacked Porous Nickel-Iron Nitride Nanosheet: A Highly Efficient Bifunctional Electrocatalyst for Overall Water Splitting, ACS Appl. Mater. Interfaces, 8, 29, 18652-18657 (2016).
[7] M. Jiang, Y. Li, Z. Lu, X. Sun, X. Duan, Binary nickel–iron nitride nanoarrays as bifunctional electrocatalysts for overall water splitting, Inorg. Chem. Front., 3, 630-634 (2016).
[8] B. Zhang, C. Xiao, S. Xie, J. Liang, X. Chen, Y. Tang, Iron–Nickel Nitride Nanostructures in Situ Grown on Surface-Redox-Etching Nickel Foam: Efficient and Ultrasustainable Electrocatalysts for Overall Water Splitting, Chem. Mater. 28, 19, 6934-6941 (2016).
[9] C. Hu, Y. Wu, Bipolar performance of the electroplated iron–nickel deposits for water electrolysis, Materials Chemistry and Physics 82, 588–596 (2003).
[10] C. G. Morales-Guio, M. T. Mayer, A. Yella, S. D. Tilley, M. Grätzel, X. Hu, An Optically Transparent Iron Nickel Oxide Catalyst for Solar Water Splitting, J. Am. Chem. Soc. 137, 9927-9936 (2015).
[11] K. Fominykh, P. Chernev, I. Zaharieva, J. Sicklinger, G. Stefanic, M. Döblinger, A. Müller, A. Pokharel, S. Böcklein, C. Scheu, T. Bein, D. Fattakhova-Rohlfing, Iron-Doped Nickel Oxide Nanocrystals as Highly Efficient Electrocatalysts for Alkaline Water Splitting, ACS Nano, 5, 5180–5188 (2015).
[12] G.Vinuesa, Estructura Electrónica y Propiedades Magnéticas de Nanoaleaciones de FeNi, Trabajo Fin de Grado, Facultad de Ciencias, Universidad de Valladolid (2018).
[13] P. Hohenberg, W. Kohn, Inhomogeneous Electron Gas, Phys. Rev. 136, B864 (1964).
[14] G. Kresse. J. Hafner, Ab initio molecular dynamics for liquid metals, Phys. Rev. B 47, 558 (1993).
[15] G. Kresse. J. Hafner, Ab initio molecular-dynamics simulation of the liquid-metal–amorphous-semiconductor transition in germanium, Phys. Rev. B 49, 14251 (1994).
[16] G. Kresse. J. Furthmüller, Efficiency of ab-initio total energy calculations for metals and semiconductors using a plane-wave basis set, Comput. Mat. Sci. 6, 15 (1996).
[17] G. Kresse. J. Hafner, Efficient iterative schemes for ab initio total-energy calculations using a plane-wave basis set, Phys. Rev. B 54, 11169 (1996).
[18] J. P. Perdew, K. Burke, M. Ernzerhof, Generalized Gradient Approximation Made Simple, Phys. Rev. Lett. 77, 3865 (1996).
[19] W. Kohn, L. J. Sham, Self-Consistent Equations Including Exchange and Correlation Effects, Phys. Rev. 140, A1133 (1965).
[20] G.Kresse, D. Joubert, From ultrasoft pseudopotentials to the projector augmented-wave method, Phys. Rev. B 59, 1758 (1999).
[21] P. E. Blöchl, Phys. Rev. B 50, 17953 (1994).
[22] C. Rostgaard, "The Projector Augmented-wave Method", (2009)
[23] R.F.W. Bader, Atoms in Molecules. A Quantum Theory, Clarendon, Oxford (1990)
[24] G. Henkelman, A. Arnaldsson, H. Jónsson, A fast and robust algorithm for Bader decomposition of charge density, Comput. Mater. Sci. 36, 354–360 (2006).
[25] P. Geerlings, F. De Proft, W. Langenaeker, Conceptual density functional theory, Chem. Rev. 103, 1793–1873 (2003).
[26] R.G. Pearson, Absolute electronegativity and hardness: application to inorganic chemistry, Inorg. Chem. 27, 734-740 (1988).
[27] P.K. Chattaraj, S. Duley, Electron affinity, electronegativity, and electrophilicity of atoms and ions, J. Chem. Eng. Data 55, 1882–1886 (2010).
[28] R.G. Parr, L. von Szentpaly, S. Liu, Electrophilicity index, J. Am. Chem. Soc. 121, 1922-1924 (1999).
[29] P. Geerlings, F. De Proft, W. Langenaeker, Conceptual density functional theory, Chem. Rev. 103, 1793-1873 (2003)

[30] W. Yang, R.G. Parr, Hardness, softness and the Fukui function in the electronic theory of metals and catalysis, Proc. Natl. Acad. Sci. U. S. A. 82, 6723-6726 (1985).
[31] P. Fuentealba, P. Pérez, R. Contreras, On the condensed Fukui function, J. Chem. Phys. 113, 2544-2551 (2000).
[32] J.P. Perdew, R.G. Parr, M. Levy, J.L. Balduz, Density functional theory for fractional particle number: derivative discontinuities of the energy, Phys. Rev. Lett. 49, 1691-1694 (1982).
[33] P. G. Alvarado-Leyva, F. Aguilera-Granja, L. C. Balbás and A. Vega, Antiferromagnetic-like coupling in the cationic iron cluster of thirteen atoms, Phys. Chem. Chem. Phys. 15, 14458-14464 (2013).

VI. SUPPLEMENTARY INFORMATION

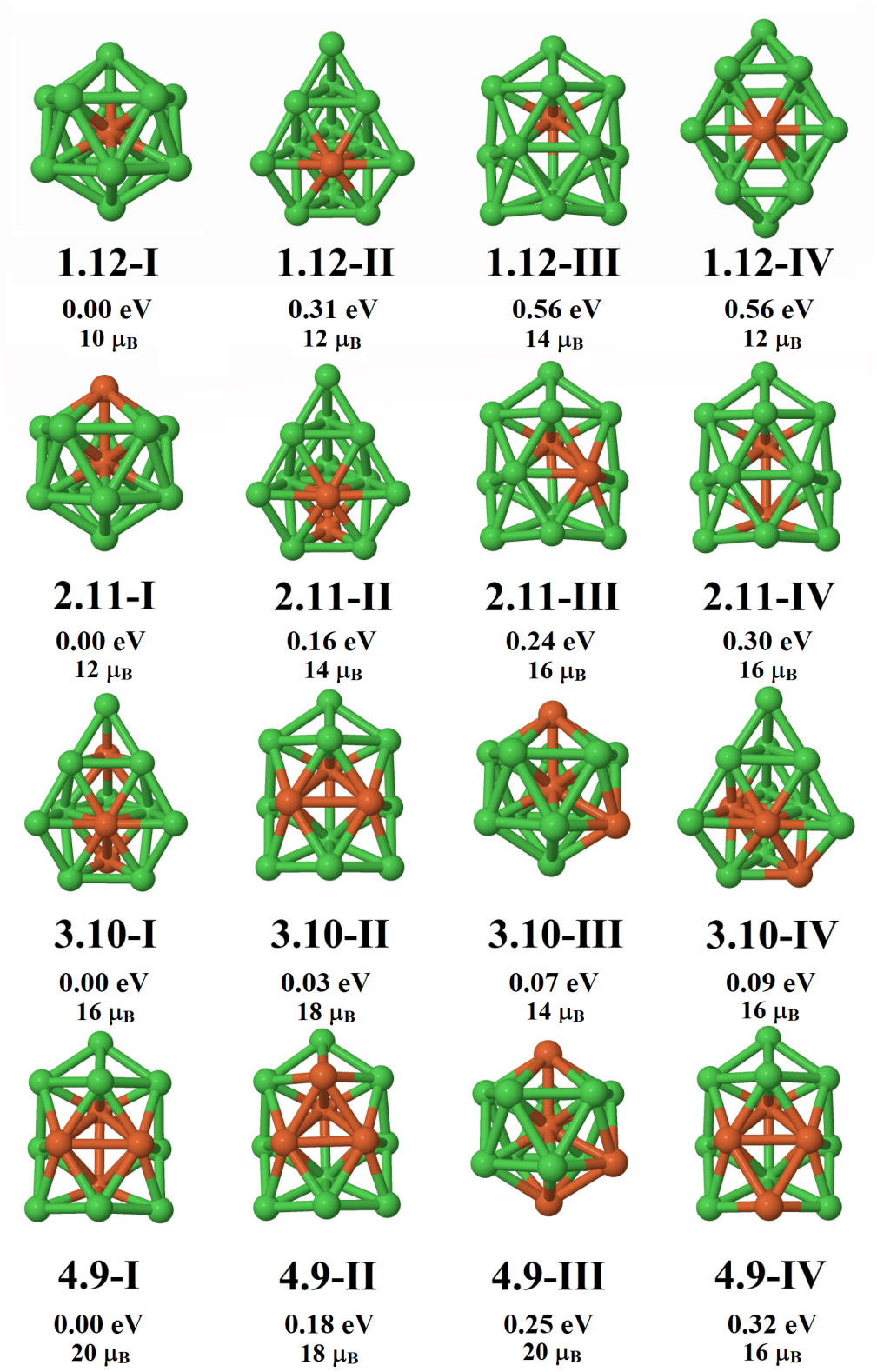

FIGURE A1: Ground state and first low-energy isomers of Fe_xNi_{13-x} nanoalloys in the $1 \leq x \leq 4$ cluster range.

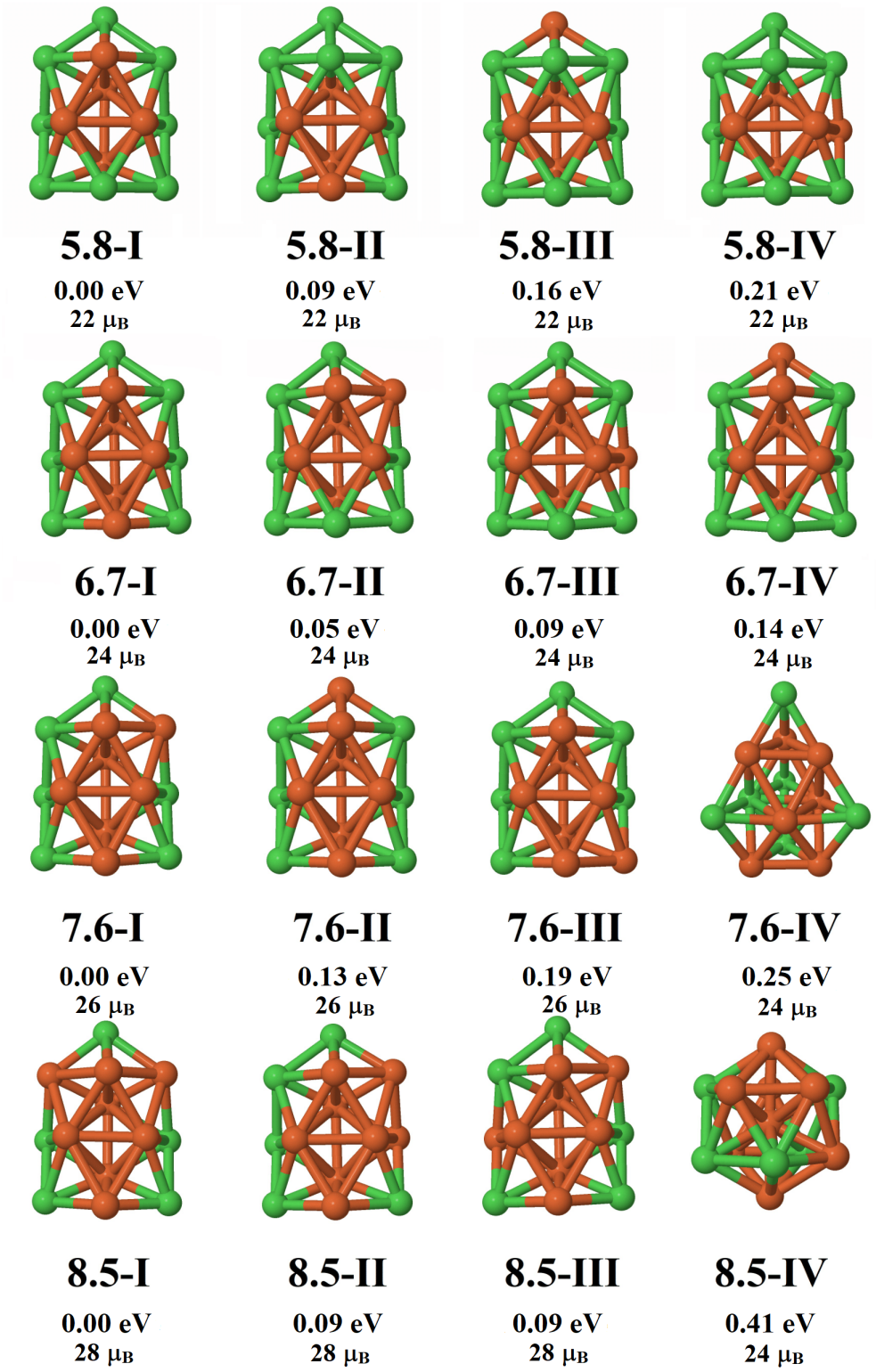

FIGURE A2: Ground state and first low-energy isomers of Fe_xNi_{13-x} nanoalloys in the $5 \leq x \leq 8$ cluster range.

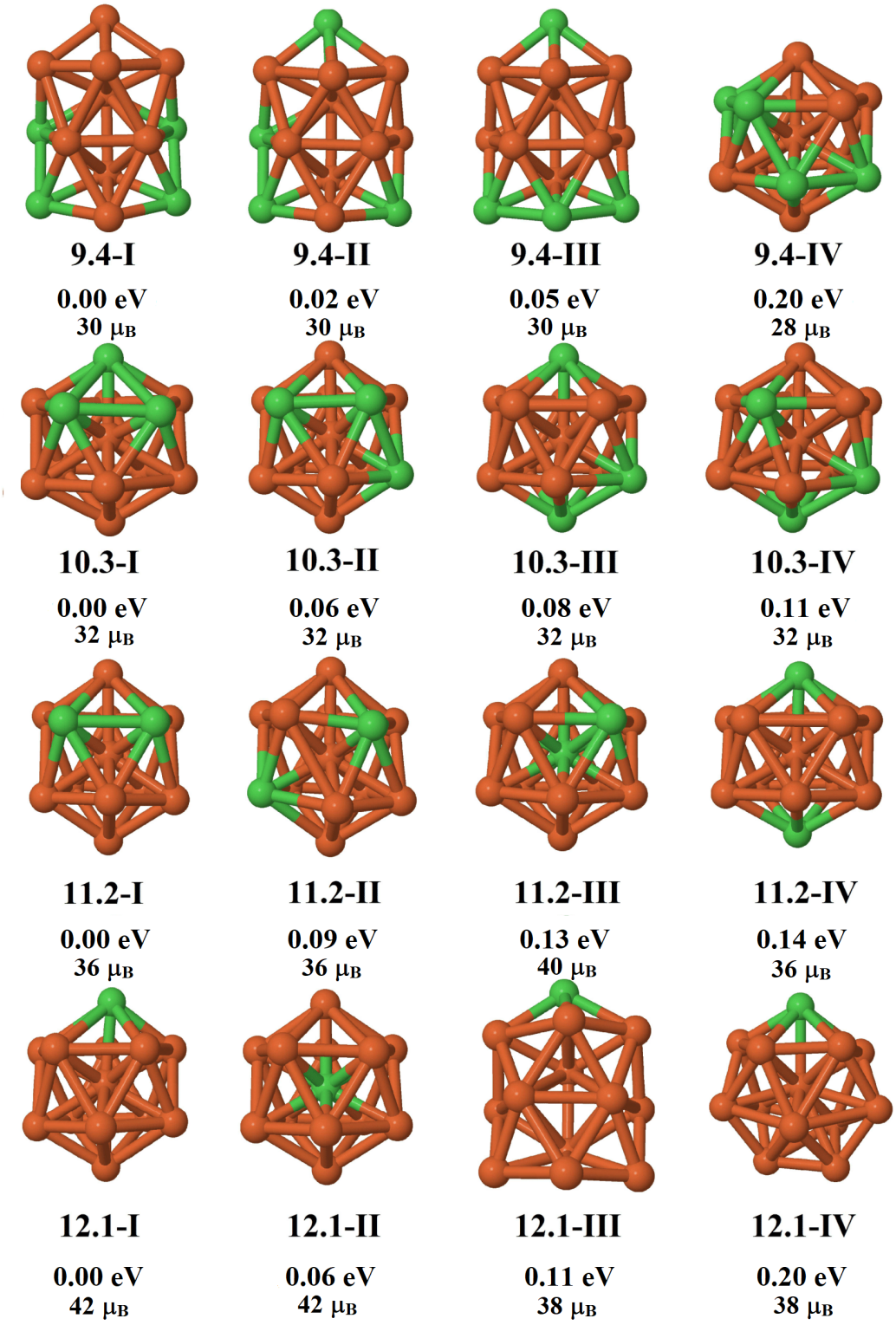

FIGURE A3: Ground state and first low-energy isomers of Fe_xNi_{13-x} nanoalloys in the $9 \leq x \leq 12$ cluster range.

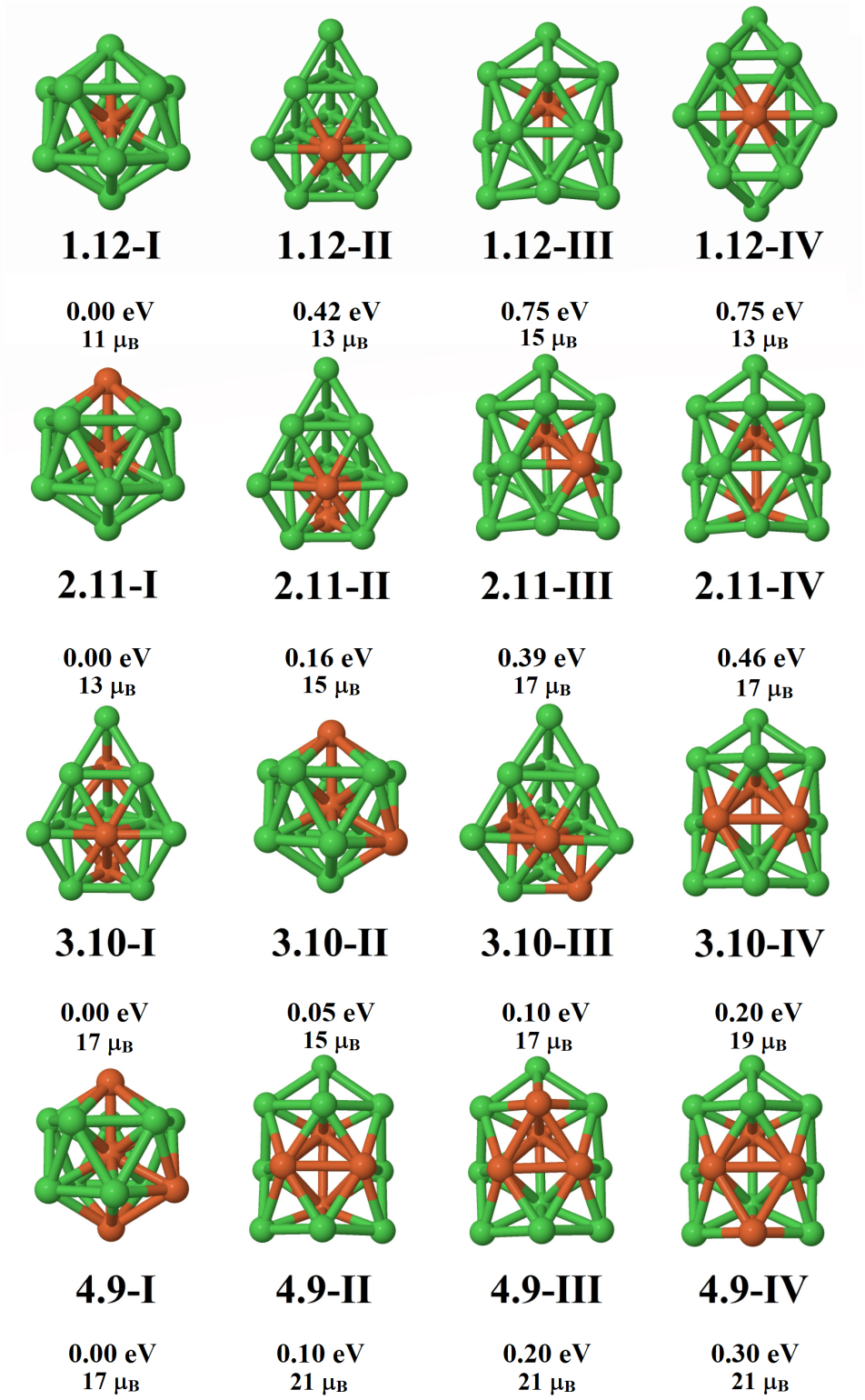

FIGURE A4: Ground state and first low-energy isomers of $Fe_xNi^+_{13-x}$ nanoalloys in the $1 \leq x \leq 4$ cluster range.

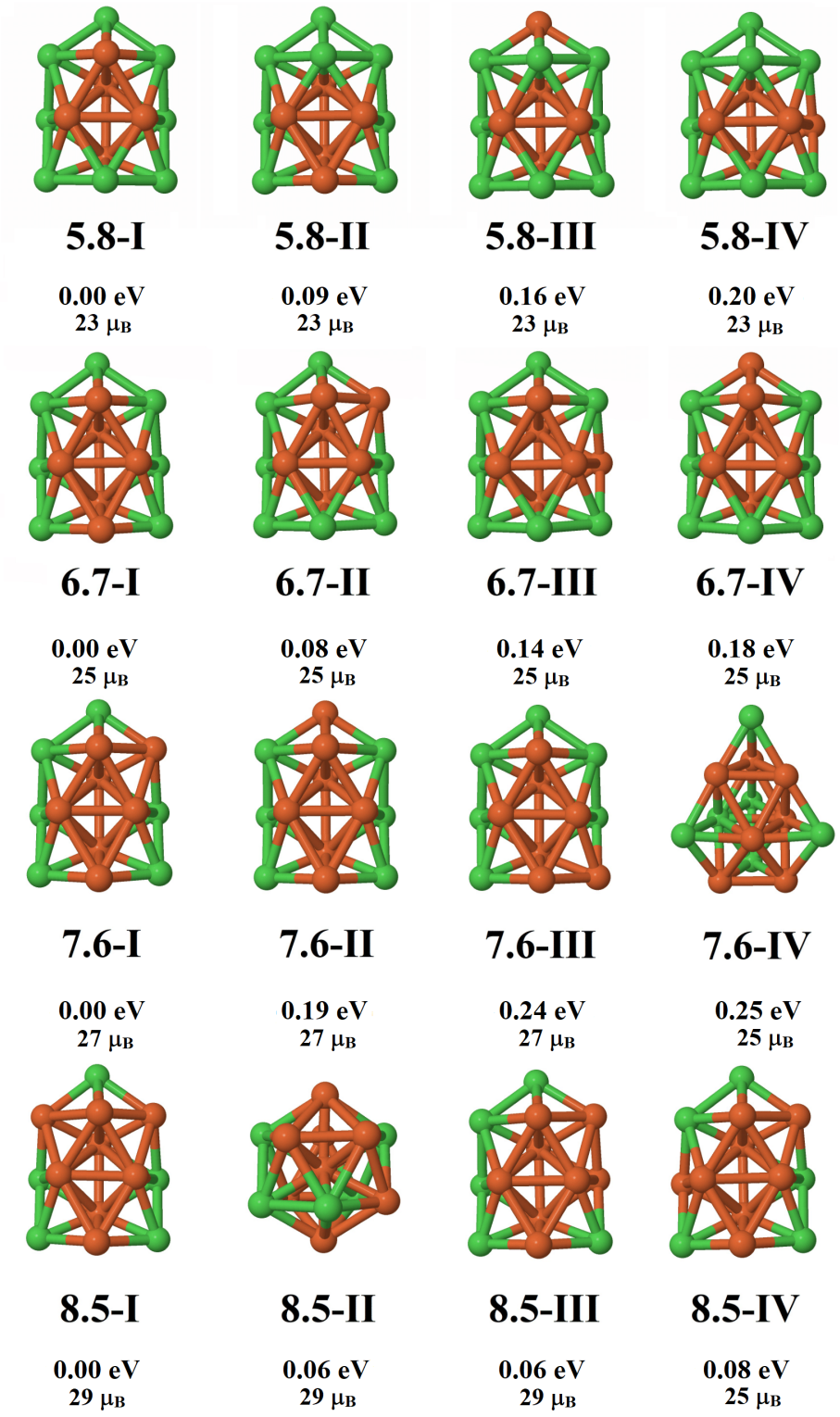

FIGURE A5: Ground state and first low-energy isomers of $Fe_xNi^+_{13-x}$ nanoalloys in the $5 \leq x \leq 8$ cluster range.

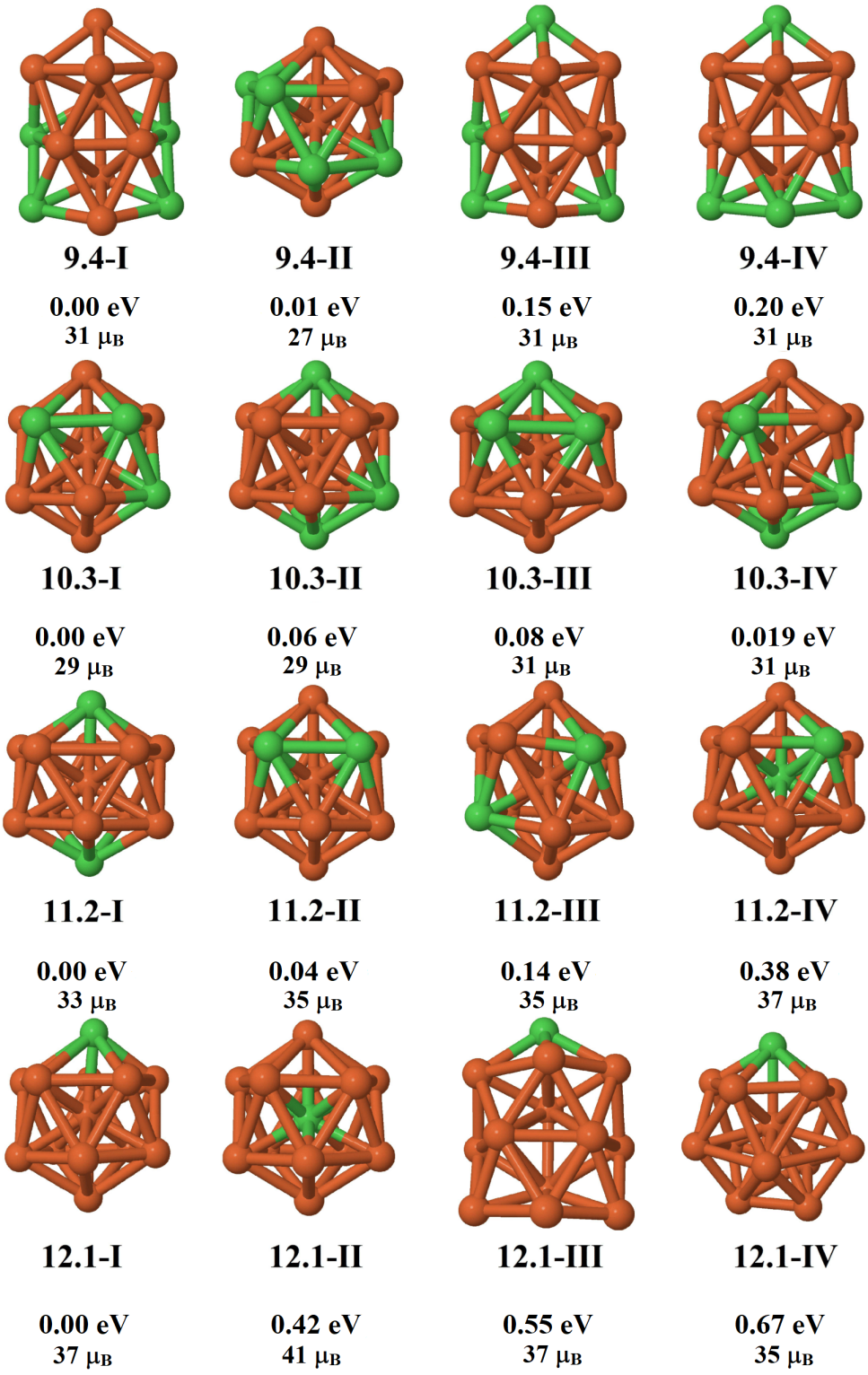

FIGURE A6: Ground state and first low-energy isomers of $Fe_xNi^+_{13-x}$ nanoalloys in the $9 \leq x \leq 12$ cluster range.

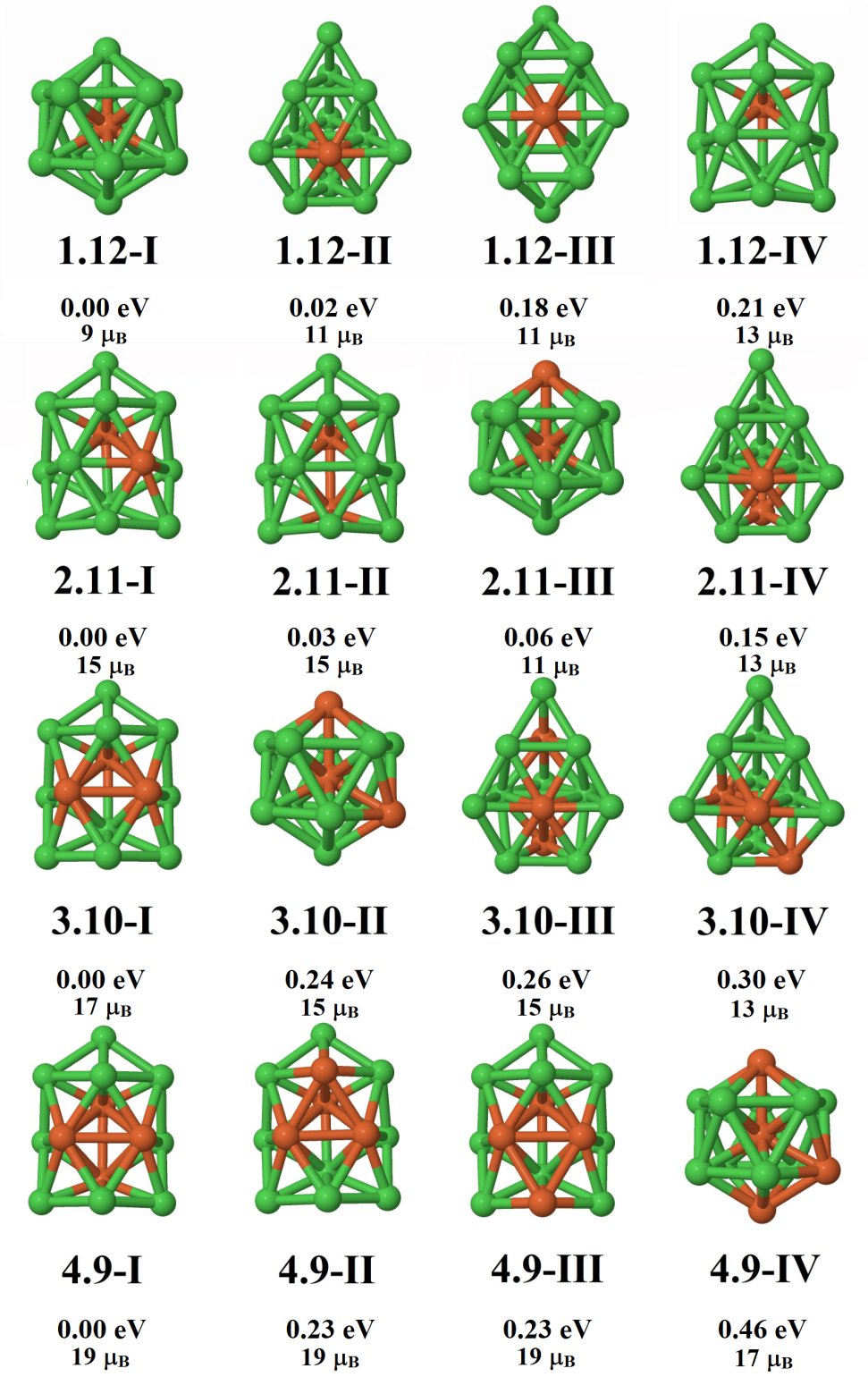

FIGURE A7: Ground state and first low-energy isomers of $Fe_xNi^-_{13-x}$ nanoalloys in the $1 \leq x \leq 4$ cluster range.

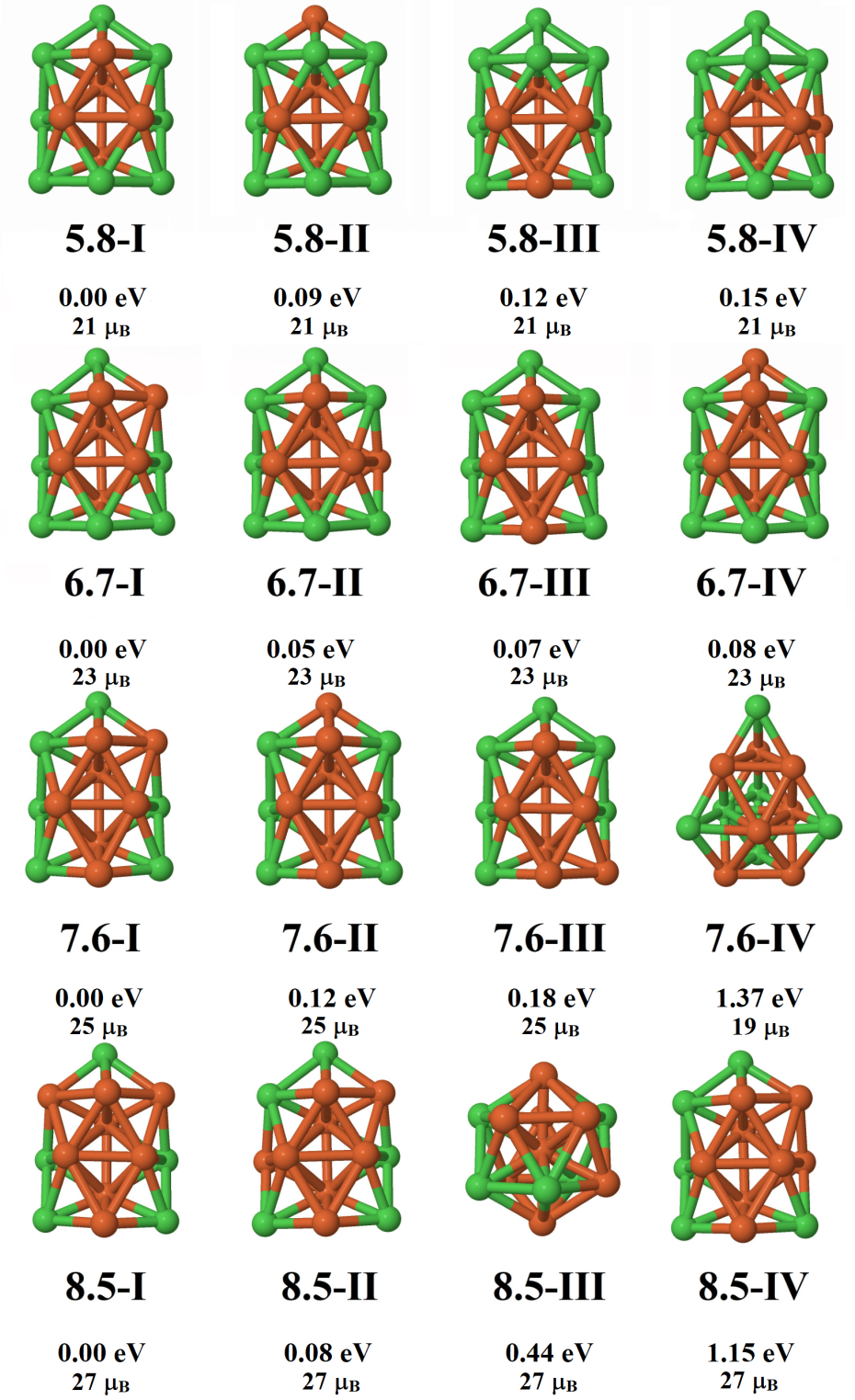

FIGURE A8: Ground state and first low-energy isomers of $Fe_xNi^-_{13-x}$ nanoalloys in the $5 \leq x \leq 8$ cluster range.

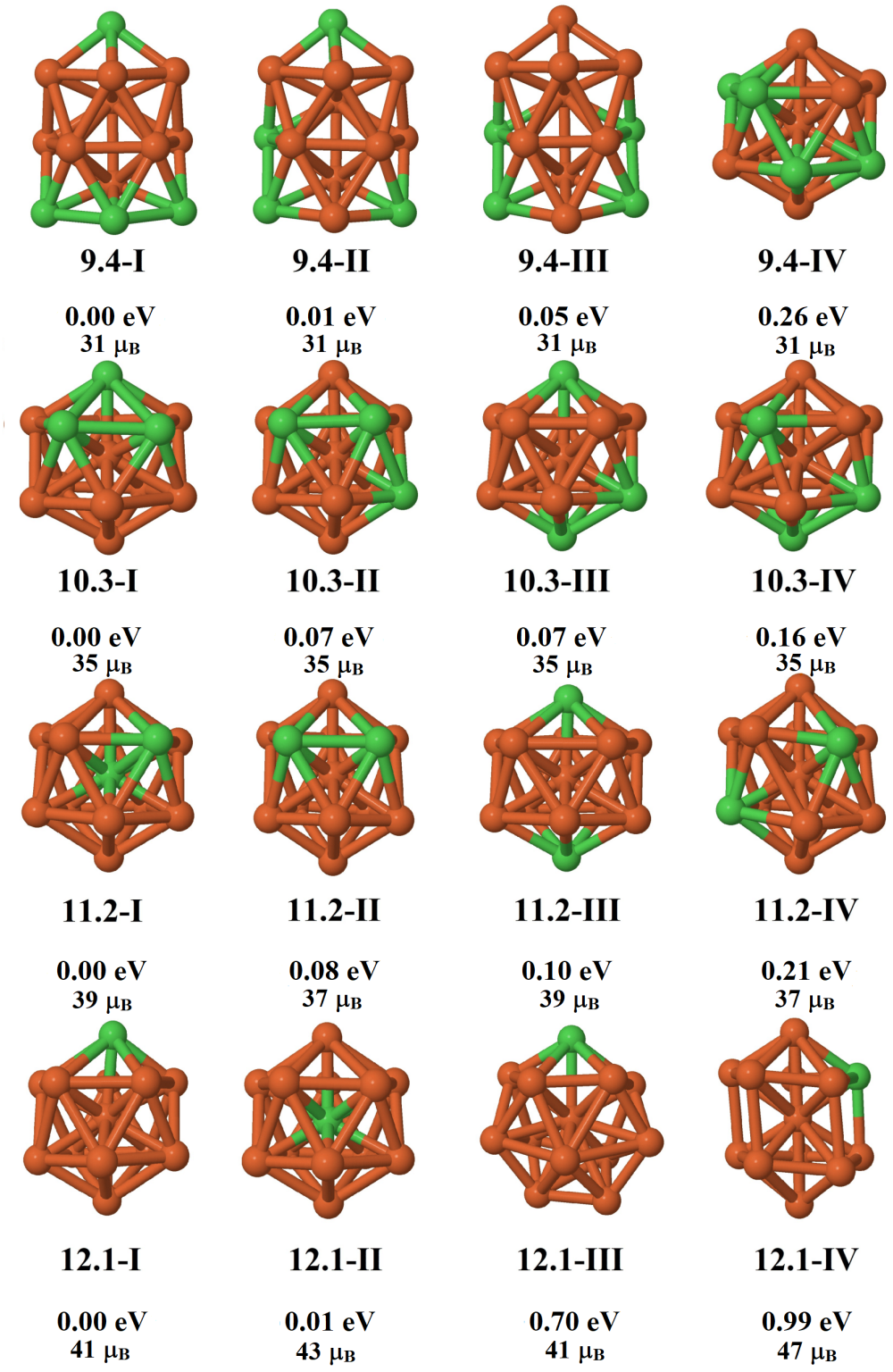

FIGURE A9: Ground state and first low-energy isomers of $Fe_xNi^-_{13-x}$ nanoalloys in the $9 \leq x \leq 12$ cluster range.

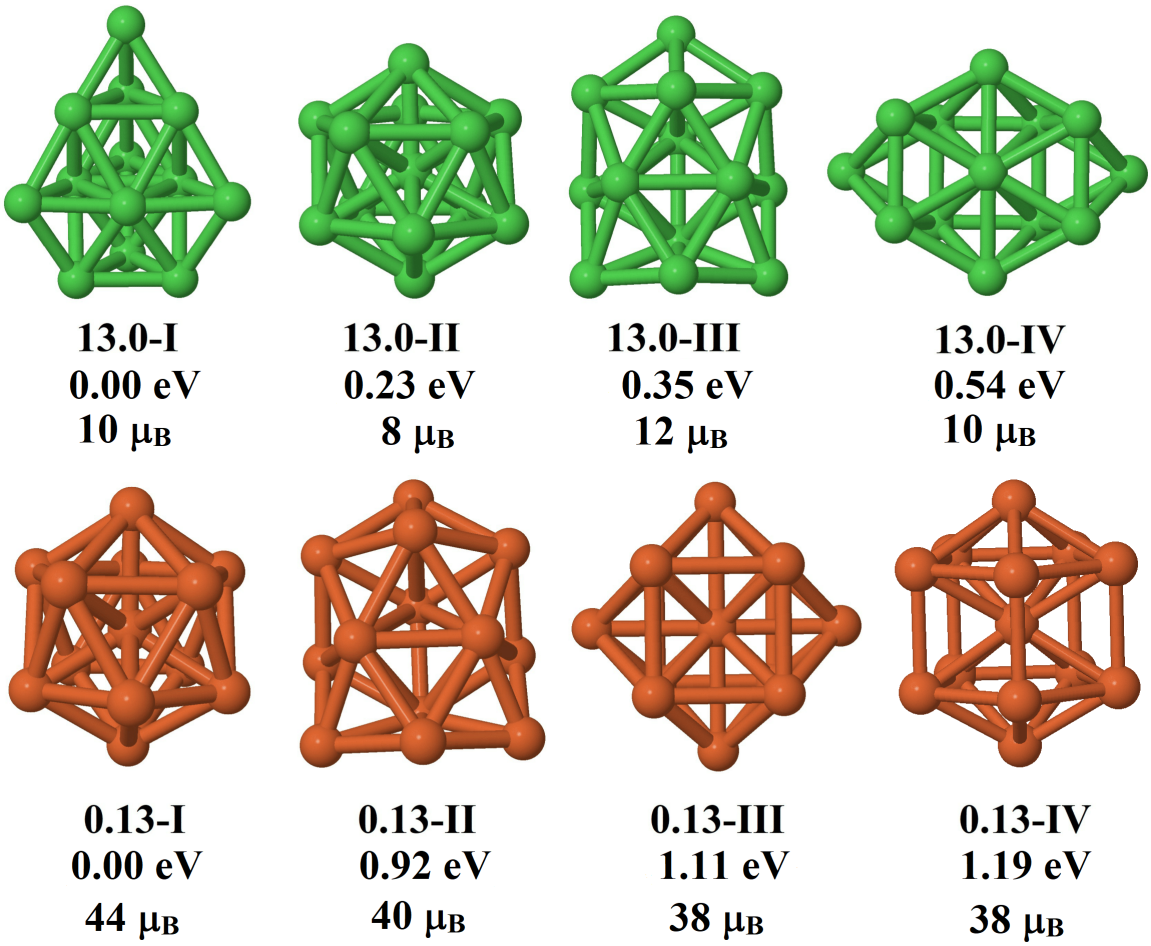

FIGURE A10: Pure Fe_{13} and Ni_{13} trial structures after ion relaxation.

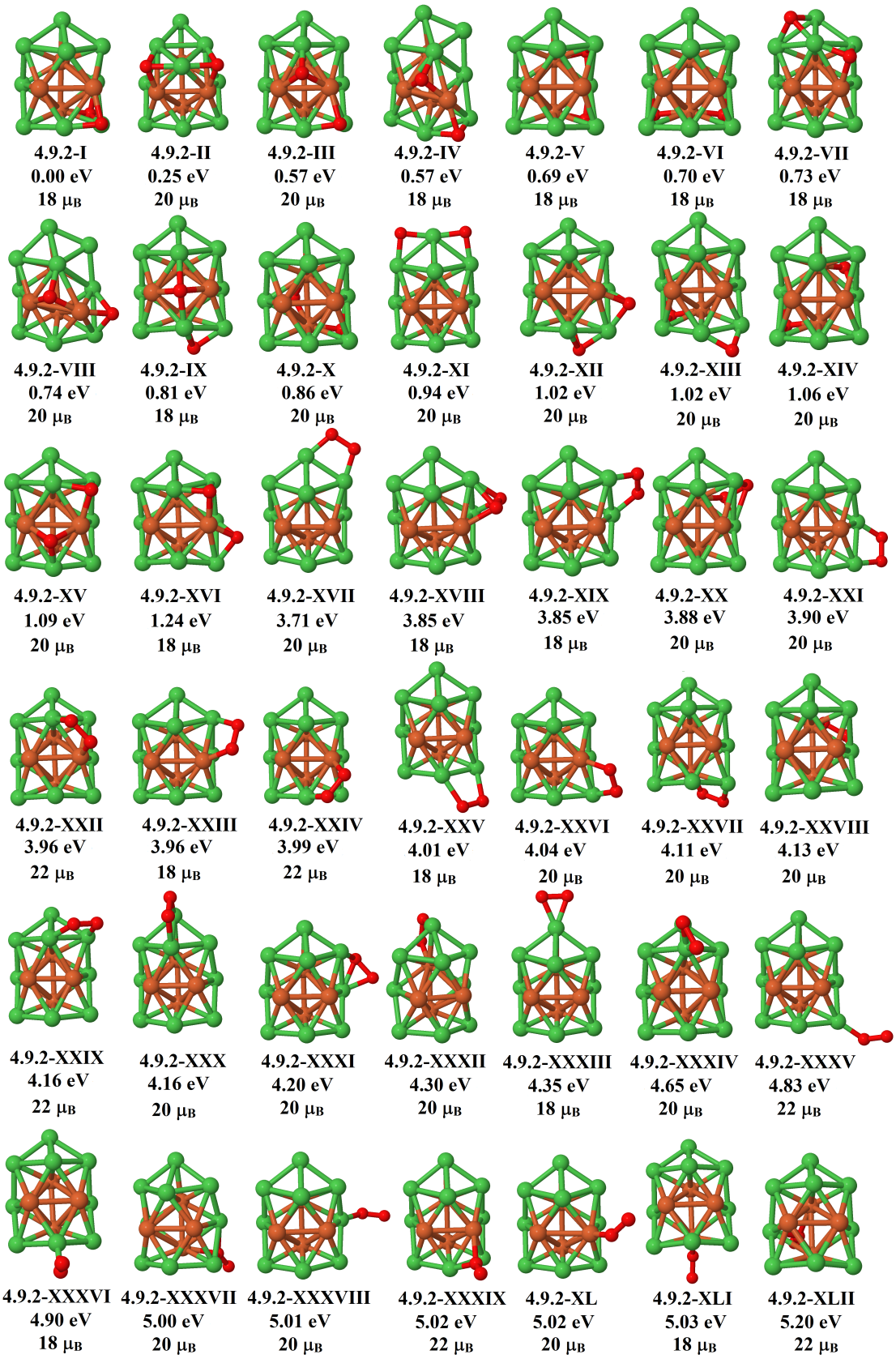

FIGURE A11: $Fe_4Ni_9O_2$ structures in order of stability.

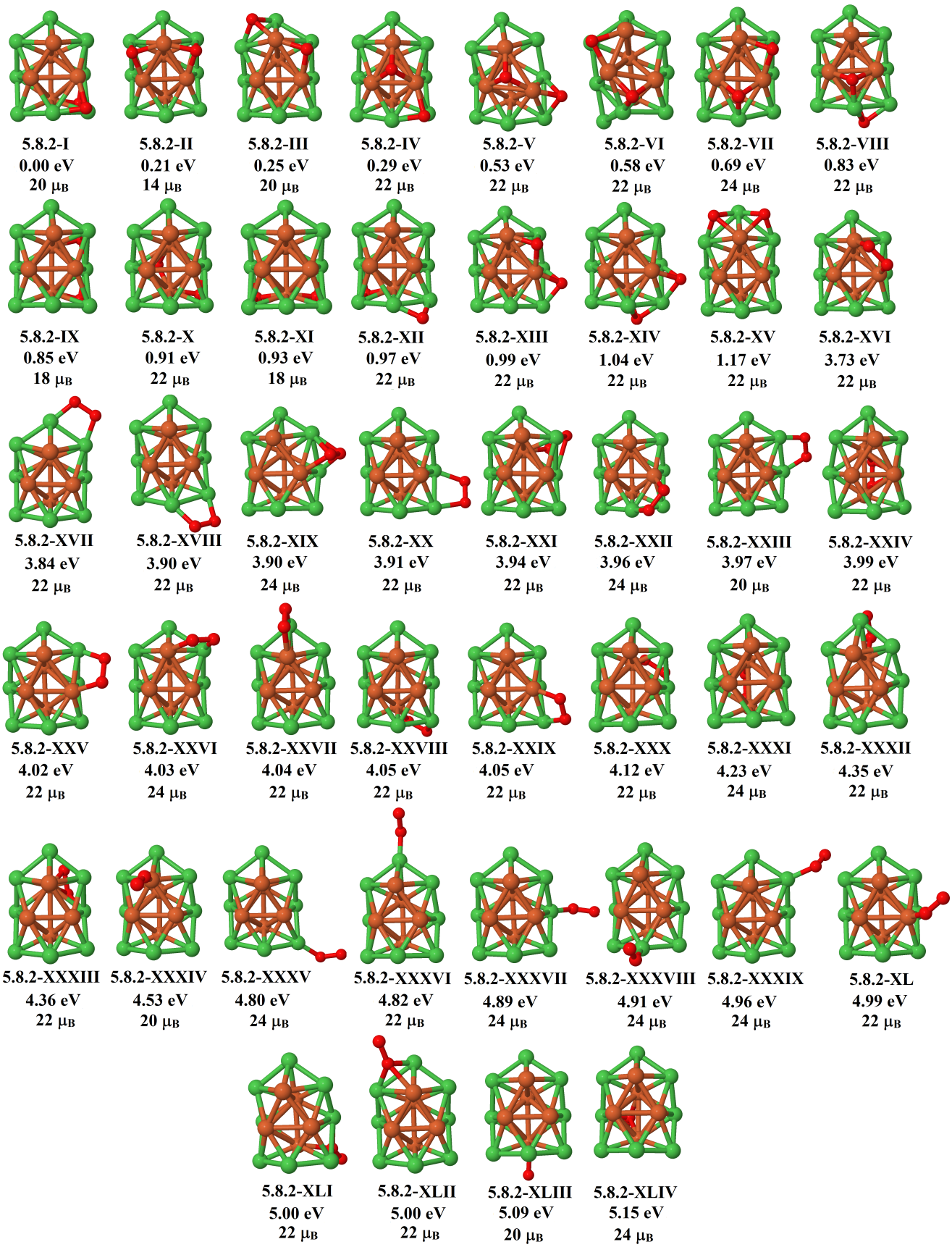

FIGURE A12: $Fe_5Ni_8O_2$ structures in order of stability.

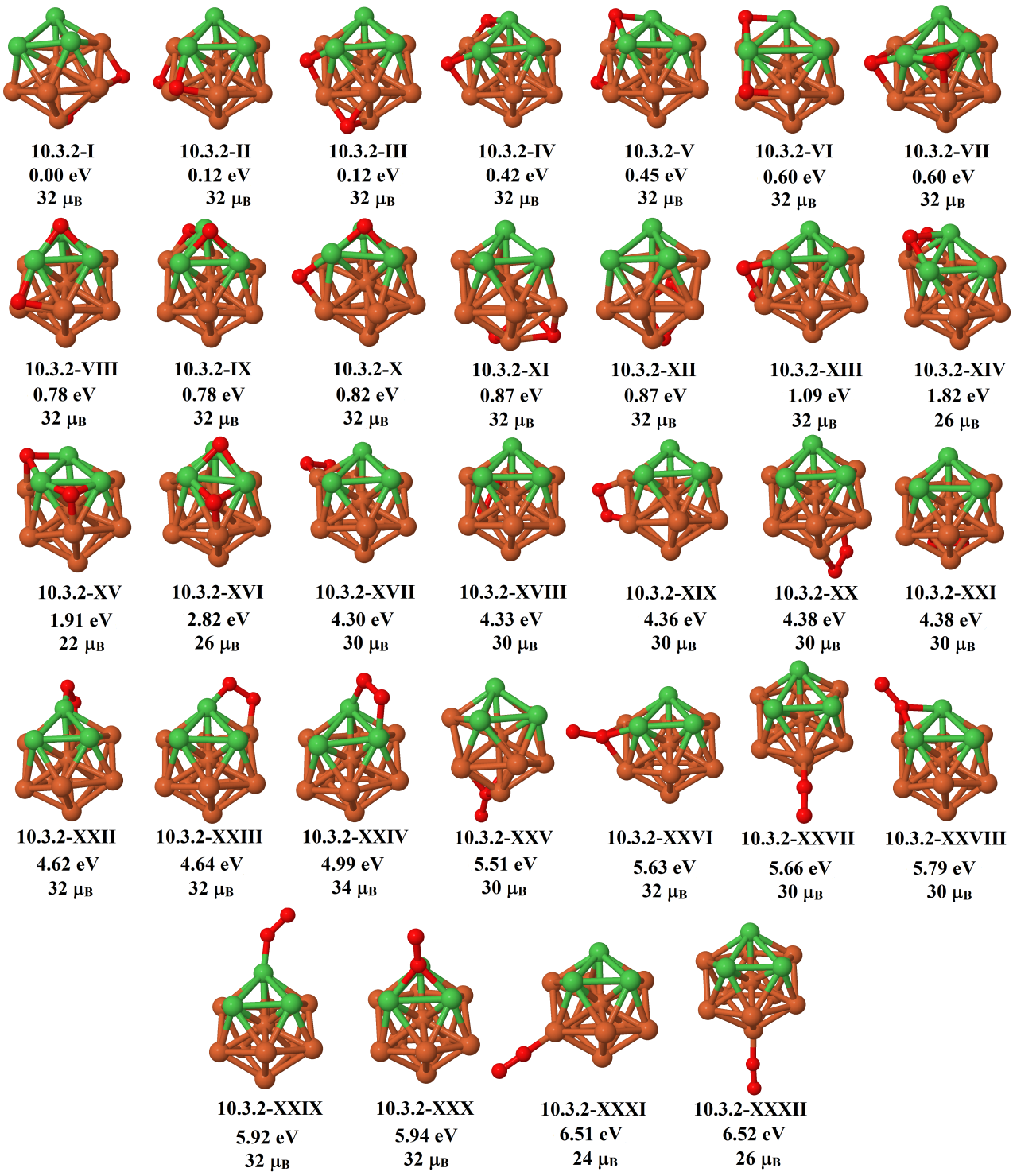

FIGURE A13: $Fe_{10}Ni_3O_2$ structures in order of stability.

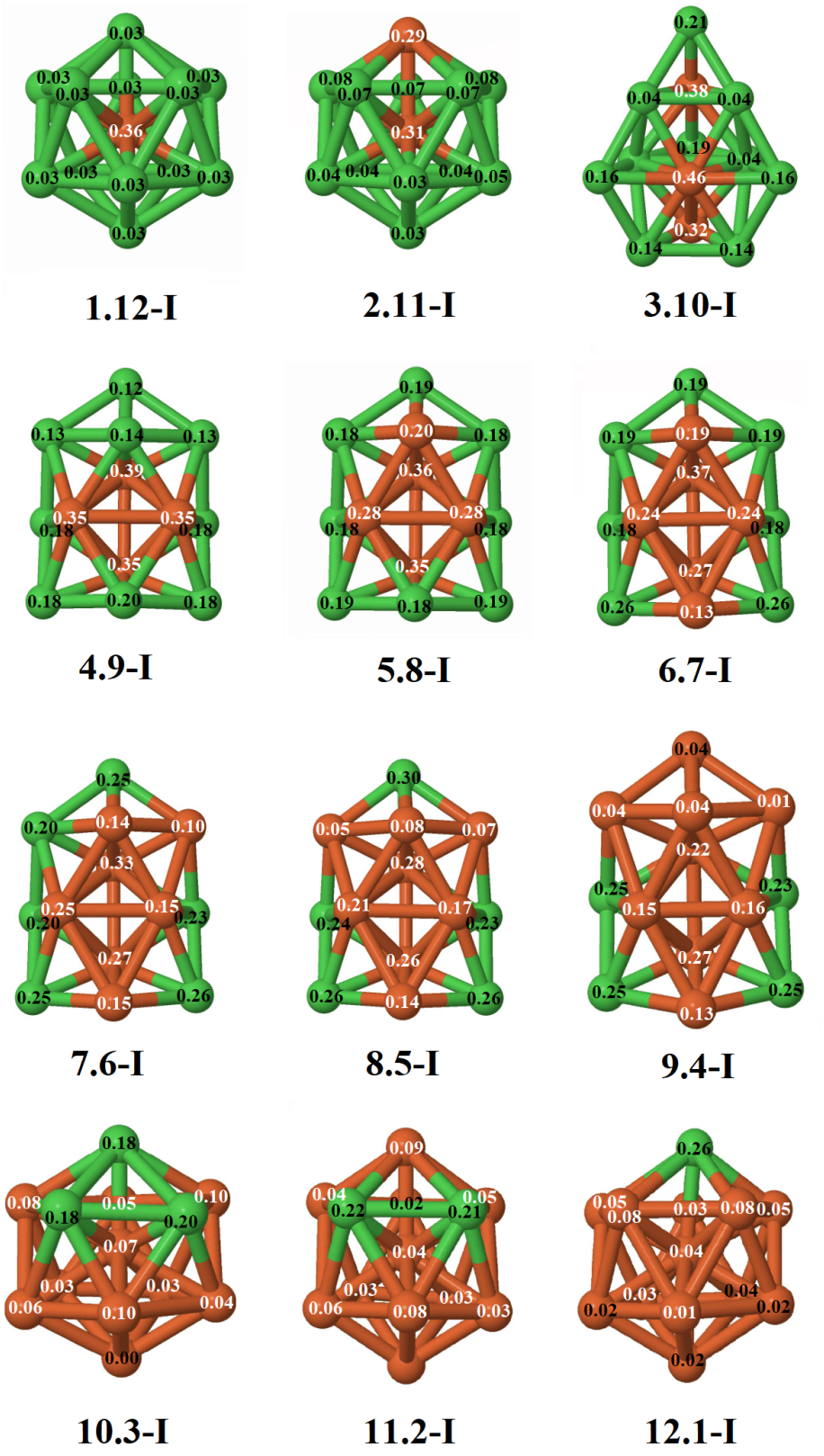

FIGURE A14: Fe_xNi_{13-x} charge transfer of the neutral GS structures. Black (white) numbers stand for gain (loss) of charge.